High-order upwind methods based on C^2-continuous two-node integrated-RBF elements for viscous flows

D.-A. An-Vo[1], N. Mai-Duy[1] and T. Tran-Cong[1]

Abstract: In this paper, 2-node integrated radial basis function elements (IRBFEs) [CMES, vol.72, no.4, pp.299-334, 2011] are further developed for the simulation of incompressible viscous flows in two dimensions. Emphasis is placed on (i) the incorporation of C^2-continuous 2-node IRBFEs into the subregion and point collocation frameworks for the discretisation of the stream function-vorticity formulation on Cartesian grids; and (ii) the development of high order upwind schemes based on 2-node IRBFEs for the case of convection-dominant flows. High levels of accuracy and efficiency of the present methods are demonstrated by solutions of several benchmark problems defined on rectangular and non-rectangular domains.

Keywords: integrated-radial-basis-function elements, Cartesian grid, control volume, subregion collocation, point collocation, local approximation, upwind scheme.

1 Introduction

Cartesian-grid-based subregion/point collocation methods can be very economical owing to the facts that (i) generating a grid and integrating the governing equations in these methods are low-cost; and (ii) FFT can be applied to accelerate computational processes, e.g. Huang and Greengard (2000). The approximations for the dependent variables and their spatial derivatives can be constructed globally on the whole grid or locally on small segments of the grid. Examples of local approximation schemes include standard control-volume (CV) methods and finite-difference methods. For the former, the fluxes are estimated by a linear variation between two grid points, e.g. Patankar (1980); Huilgol and Phan-Thien (1997). The use of two grid points allows for the consistency of the fluxes at CV faces - one of the four basic rules to guarantee a physically realistic solution (Patankar (1980)). For the latter, local approximations can be constructed in each direction independently using two nodes (first-order accuracy) and three nodes (second-order accuracy). With two-

[1] Computational Engineering and Science Research Centre, Faculty of Engineering and Surveying, The University of Southern Queensland, Toowoomba, QLD 4350, Australia

node-based local approximations, Cartesian grid based methods typically produce solutions which are continuous for the fields but not for their partial derivatives, i.e. C^0 continuity. The grid thus needs to be sufficiently fine to mitigate the effects of discontinuity of partial derivatives.

The Navier-Stokes (N-S) equations involve two main terms, namely convection and diffusion. At high values of the Reynold number, the convection term is dominant and the numerical simulation of the N-S equations becomes challenging. Various treatments for the convection term have been proposed in the literature. Those which take the influence of the upstream information of the flow into account, e.g. the upwind differencing (Courant, Isaccson, and Rees (1952); Gentry, Martin, and Daly (1966)), hybrid (Spalding (1972)), power-law (Patankar (1981)) and QUICK (Leonard (1979)) schemes are known to provide a very stable solution. To maintain a high level of accuracy, an effective way is to employ high-order upwind schemes with the deferred-correction strategy, e.g. Khosla and Rubin (1974); Ghia, Ghia, and Shin (1982).

Radial basis functions (RBFs) have been successfully used for the approximation of scattered data. They have recently emerged as an attractive tool for the solution of ordinary and partial differential equations (ODEs and PDEs), e.g. Fasshauer (2007); Atluri and Shen (2002); Chen, Karageorghis, and Smyrlis (2008). RBF-based approximants are able to produce fast convergence especially for regular node arrangements such as those based on Cartesian grids. They can be constructed through a conventional differentiation process, e.g. Kansa (1990), or an integration process, e.g. Mai-Duy and Tran-Cong (2001); Mai-Duy and Tanner (2005); Mai-Duy and Tran-Cong (2005). The latter helps avoid the reduction of convergence rate caused by differentiation and provide effective ways of imposing the derivative boundary values. RBF-based approximants can be constructed globally or locally. Global RBF-based methods are very accurate, e.g. Cheng, Golberg, Kansa, and Zammito (2003); Huang, Lee, and Cheng (2007). However, they result in a system matrix that is dense and usually highly ill-conditioned. The use of RBF-approximants in local forms has the ability to circumvent these difficulties, e.g. Shu, Ding, and Yeo (2003); Šarler and Vertnik (2006); Divo and Kassab (2007). Recently, a local high order approximant based on 2-node elements and integrated RBFs (IRBFs) for solving second-order elliptic problems in the CV framework has been proposed by An-Vo, Mai-Duy, and Tran-Cong (2011). In such 2-node elements (IRBFEs), the integration constants are exploited to include the first derivatives at the element extremes in the approximations. It was shown that such elements lead to a C^2-continuous solution rather than the usual C^0-continuous solution.

In this study, C^2-continuous 2-node IRBFEs are incorporated into the subregion and

point collocation frameworks for solving the N-S equations in the stream function-vorticity formulation on Cartesian grids. Unlike conventional finite-element-based methods, the proposed methods can guarantee inter-element continuity of derivatives of the stream function and vorticity of orders up to 2. At high values of the Reynolds number, to achieve both good accuracy and stability properties, several high-order upwind schemes are proposed. The resultant system of algebraic equations is sparse and banded; the solution accuracy can be controlled by means of the number of RBFs and/or the shape parameter. Several viscous flows defined on rectangular and non-rectangular domains are considered to verify the proposed methods.

The remainder of the paper is organised as follows. Brief reviews of the governing equations and integrated RBF elements are given in Section 2 and 3, respectively. Section 4 describes the proposed C^2-continuous subregion/point collocation techniques for the stream function-vorticity formulation. In Section 5, two benchmark problems, namely the lid-driven cavity flow and the flow past a circular cylinder in a channel, are presented to demonstrate the attractiveness of the present techniques. Section 6 concludes the paper.

2 Governing equations

The dimensionless N-S equations for steady incompressible planar viscous flows, subject to negligible body forces, can be expressed in terms of the stream function ψ and the vorticity ω as follows

$$\frac{\partial^2\psi}{\partial x^2}+\frac{\partial^2\psi}{\partial y^2}+\omega=0, \tag{1}$$

$$\frac{\partial^2\omega}{\partial x^2}+\frac{\partial^2\omega}{\partial y^2}=Re\left(\frac{\partial\psi}{\partial y}\frac{\partial\omega}{\partial x}-\frac{\partial\psi}{\partial x}\frac{\partial\omega}{\partial y}\right), \qquad (x,y)^T\in\Omega, \tag{2}$$

where $Re=UL/\nu$ is the Reynolds number, in which L is the characteristic length, U the characteristic speed of the flow and ν the kinematic viscosity. The vorticity and stream function variables are defined by

$$\omega=\frac{\partial v}{\partial x}-\frac{\partial u}{\partial y}, \tag{3}$$

$$\frac{\partial\psi}{\partial y}=u, \quad \frac{\partial\psi}{\partial x}=-v, \tag{4}$$

where u and v are the x and y components of the velocity vector. In this study, the method of modified dynamics or false transients (e.g. Mallinson and Davis (1973);

Pozrikidis (1997)) is applied to obtain the structure of a steady flow. The governing equations (1) and (2) are modified as

$$\frac{\partial^2\psi}{\partial x^2}+\frac{\partial^2\psi}{\partial y^2}+\omega=\frac{\partial\psi}{\partial t}, \tag{5}$$

$$\frac{\partial^2\omega}{\partial x^2}+\frac{\partial^2\omega}{\partial y^2}-Re\left(\frac{\partial\psi}{\partial y}\frac{\partial\omega}{\partial x}-\frac{\partial\psi}{\partial x}\frac{\partial\omega}{\partial y}\right)=\frac{\partial\omega}{\partial t}. \tag{6}$$

Solutions to (5) and (6), which are obtained from integrating the equations from a given initial condition up to the steady state, are also solutions to (1) and (2) respectively.

In the case of subregion collocation, one needs to define control volumes for grid nodes. Integrating (5) and (6) over a CV of a grid point P, Ω_P, leads to the following equations

$$\int_{\Omega_P}\left(\frac{\partial^2\psi}{\partial x^2}+\frac{\partial^2\psi}{\partial y^2}\right)\mathrm{d}\Omega_P+\int_{\Omega_P}\omega\mathrm{d}\Omega_P=\int_{\Omega_P}\frac{\partial\psi}{\partial t}\mathrm{d}\Omega_P, \tag{7}$$

$$\int_{\Omega_P}\left(\frac{\partial^2\omega}{\partial x^2}+\frac{\partial^2\omega}{\partial y^2}\right)\mathrm{d}\Omega_P-\int_{\Omega_P}Re\left(\frac{\partial\psi}{\partial y}\frac{\partial\omega}{\partial x}-\frac{\partial\psi}{\partial x}\frac{\partial\omega}{\partial y}\right)\mathrm{d}\Omega_P=\int_{\Omega_P}\frac{\partial\omega}{\partial t}\mathrm{d}\Omega_P, \tag{8}$$

which ensure that the flow field is conservative for a finite CV.
Applying the Green theorem to (7) and (8), one has

$$\oint_{\Gamma_P}\left(\frac{\partial\psi}{\partial x}\mathrm{d}y-\frac{\partial\psi}{\partial y}\mathrm{d}x\right)+\int_{\Omega_P}\omega\mathrm{d}\Omega_P=\int_{\Omega_P}\frac{\partial\psi}{\partial t}\mathrm{d}\Omega_P, \tag{9}$$

$$\oint_{\Gamma_P}\left[\left(\frac{\partial\omega}{\partial x}-Re\,\omega\frac{\partial\psi}{\partial y}\right)\mathrm{d}y-\left(\frac{\partial\omega}{\partial y}+Re\,\omega\frac{\partial\psi}{\partial x}\right)\mathrm{d}x\right]=\int_{\Omega_P}\frac{\partial\omega}{\partial t}\mathrm{d}\Omega_P, \tag{10}$$

where Γ_P is the CV boundary. The governing differential equations (5) and (6) are thus transformed into a CV form (7)-(8) or (9)-(10). It is noted that no approximation is made at this stage.

3 Definition of integrated-RBF elements

3.1 Brief review of integrated RBFs

For a given ODE/PDE, the integrated-RBF approach consists in decomposing highest-order derivatives in the ODE/PDE into RBFs and then integrating these RBFs to yield expressions for lower-order derivatives and finally the original function itself Mai-Duy and Tran-Cong (2003). In the case of second-order ODEs/PDEs such as (1) and (2), integrated-RBF expressions employed with the multiquadric (MQ)

function are given by

$$\frac{\partial^2\phi}{\partial\eta^2}(\mathbf{x}) = \sum_{i=1}^{n} w_i \sqrt{(\mathbf{x}-\mathbf{c}_i)^2 + a_i^2} = \sum_{i=1}^{n} w_i I_i^{(2)}(\mathbf{x}), \qquad \mathbf{x} \in \Omega, \tag{11}$$

$$\frac{\partial\phi}{\partial\eta}(\mathbf{x}) = \sum_{i=1}^{n} w_i I_i^{(1)}(\mathbf{x}) + C_1(\theta), \tag{12}$$

$$\phi(\mathbf{x}) = \sum_{i=1}^{n} w_i I_i^{(0)}(\mathbf{x}) + C_1(\theta)\eta + C_2(\theta), \tag{13}$$

where Ω is the domain of interest, ϕ a function, (η,θ) the two components of $\mathbf{x}$, n the number of RBFs, $\{w_i\}_{i=1}^n$ the set of RBF weights, $C_1(\theta)$ and $C_2(\theta)$ the constants of integration which are functions of θ, $I_i^{(2)}(\mathbf{x})$ conveniently denotes the MQ whose centre and shape parameter are, respectively, $\mathbf{c}_i$ and a_i, $I_i^{(1)}(\mathbf{x}) = \int I_i^{(2)}(\mathbf{x})d\eta$, and $I_i^{(0)}(\mathbf{x}) = \int I_i^{(1)}(\mathbf{x})d\eta$. Explicit forms of $I_i^{(1)}(\mathbf{x})$ and $I_i^{(0)}(\mathbf{x})$ can be found in Mai-Duy and Tran-Cong (2001). In Mai-Duy and Tran-Cong (2003), the shape parameter was simply chosen as $a_i = \beta h_i$ in which β is a given positive number and h_i the distance between $\mathbf{c}_i$ and its nearest neighbour.

When the analysis domain Ω is a line segment, e.g. in the Cartesian direction η, expressions (11), (12) and (13) reduce to

$$\frac{\partial^2\phi}{\partial\eta^2}(\eta) = \frac{\mathrm{d}^2\phi}{\mathrm{d}\eta^2} = \sum_{i=1}^{n} w_i \sqrt{(\eta-c_i)^2 + a_i^2} = \sum_{i=1}^{n} w_i I_i^{(2)}(\eta), \tag{14}$$

$$\frac{\partial\phi}{\partial\eta}(\eta) = \frac{\mathrm{d}\phi}{\mathrm{d}\eta} = \sum_{i=1}^{n} w_i I_i^{(1)}(\eta) + C_1, \tag{15}$$

$$\phi(\eta) = \sum_{i=1}^{n} w_i I_i^{(0)}(\eta) + C_1\eta + C_2, \tag{16}$$

where C_1 and C_2 are simply constant values.

Expressions (14), (15) and (16), called 1D-IRBFs, can also be used in conjunction with Cartesian grids for solving 2D problems. Advantages of 1D-IRBFs over 2D-IRBFs ((11)-(13)) are that they possess some "local" properties and are constructed with a much lower cost. However, numerical experiments show that 1D-IRBFs still cannot work with large values of β. In An-Vo, Mai-Duy, and Tran-Cong (2011), 1D-IRBF-based schemes were further localised to 2-node IRBF elements (IRBFEs).

3.1.1 Two-node IRBFEs

These elements are applicable to problems defined on rectangular and non-rectangular domains. The problem domain is simply discretised by using a Cartesian grid. In

the case of non-rectangular domain, grid points outside the problem domain are removed while grid points inside the problem domain are taken to be interior nodes. Boundary nodes are defined as the intersection of the grid lines and the boundaries. Over straight-line segments between two adjacent nodal points, 1D-IRBFs are utilised to represent the variation of the field variable and its derivatives, which are called 2-node IRBFEs. It can be seen that there are two types of elements, namely interior and semi-interior elements. An interior element is formed using two adjacent interior nodes while a semi-interior element is generated by an interior node and a boundary node (Fig. 1).

3.1.2 Interior elements

1D-IRBF expressions for interior elements are of similar forms. Consider an interior element, $\eta \in [\eta_1, \eta_2]$, and its two nodes are locally named as 1 and 2. Let $\phi(\eta)$ be a function and ϕ_1, $\partial\phi_1/\partial\eta$, ϕ_2 and $\partial\phi_2/\partial\eta$ be the values of ϕ and $\partial\phi/\partial\eta$ at the two nodes, respectively (Fig. 2). The 2-node IRBFE scheme approximates $\phi(\eta)$ using two MQs whose centres are located at η_1 and η_2. Expressions (14), (15) and (16) become

$$\frac{\partial^2\phi}{\partial\eta^2}(\eta) = w_1\sqrt{(\eta-c_1)^2+a_1^2} + w_2\sqrt{(\eta-c_2)^2+a_2^2} = w_1 I_1^{(2)}(\eta) + w_2 I_2^{(2)}(\eta), \tag{17}$$

$$\frac{\partial\phi}{\partial\eta}(\eta) = w_1 I_1^{(1)}(\eta) + w_2 I_2^{(1)}(\eta) + C_1, \tag{18}$$

$$\phi(\eta) = w_1 I_1^{(0)}(\eta) + w_2 I_2^{(0)}(\eta) + C_1\eta + C_2, \tag{19}$$

where $I_i^{(1)}(\eta) = \int I_i^{(2)}(\eta)d\eta$, $I_i^{(0)}(\eta) = \int I_i^{(1)}(\eta)d\eta$ with $i = (1,2)$, and C_1 and C_2 are the constants of integration. By collocating (19) and (18) at η_1 and η_2, the relation between the physical space and the RBF coefficient space is obtained

$$\underbrace{\begin{pmatrix} \phi_1 \\ \phi_2 \\ \frac{\partial\phi_1}{\partial\eta} \\ \frac{\partial\phi_2}{\partial\eta} \end{pmatrix}}_{\widehat{\phi}} = \underbrace{\begin{pmatrix} I_1^{(0)}(\eta_1) & I_2^{(0)}(\eta_1) & \eta_1 & 1 \\ I_1^{(0)}(\eta_2) & I_2^{(0)}(\eta_2) & \eta_2 & 1 \\ I_1^{(1)}(\eta_1) & I_2^{(1)}(\eta_1) & 1 & 0 \\ I_1^{(1)}(\eta_2) & I_2^{(1)}(\eta_2) & 1 & 0 \end{pmatrix}}_{\mathscr{I}} \underbrace{\begin{pmatrix} w_1 \\ w_2 \\ C_1 \\ C_2 \end{pmatrix}}_{\widehat{w}}, \tag{20}$$

where $\widehat{\phi}$ is the nodal-value vector, $\mathscr{I}$ the conversion matrix, and $\widehat{w}$ the coefficient vector. It is noted that not only the nodal values of ϕ but also of $\partial\phi/\partial\eta$ are incorporated into the conversion system and this imposition is done in an exact manner

owing to the presence of integration constants. Solving (20) yields

$$\widehat{w} = \mathscr{I}^{-1}\widehat{\phi}. \tag{21}$$

Substitution of (21) into (19), (18) and (17) leads to

$$\phi(\eta) = \left[I_1^{(0)}(\eta), I_2^{(0)}(\eta), \eta, 1\right] \mathscr{I}^{-1}\widehat{\phi}, \tag{22}$$

$$\frac{\partial\phi}{\partial\eta}(\eta) = \left[I_1^{(1)}(\eta), I_2^{(1)}(\eta), 1, 0\right] \mathscr{I}^{-1}\widehat{\phi}, \tag{23}$$

$$\frac{\partial^2\phi}{\partial\eta^2}(\eta) = \left[I_1^{(2)}(\eta), I_2^{(2)}(\eta), 0, 0\right] \mathscr{I}^{-1}\widehat{\phi}. \tag{24}$$

They can be rewritten in the form

$$\phi(\eta) = \varphi_1(\eta)\phi_1 + \varphi_2(\eta)\phi_2 + \varphi_3(\eta)\frac{\partial\phi_1}{\partial\eta} + \varphi_4(\eta)\frac{\partial\phi_2}{\partial\eta}, \tag{25}$$

$$\frac{\partial\phi}{\partial\eta}(\eta) = \frac{\mathrm{d}\varphi_1(\eta)}{\mathrm{d}\eta}\phi_1 + \frac{\mathrm{d}\varphi_2(\eta)}{\mathrm{d}\eta}\phi_2 + \frac{\mathrm{d}\varphi_3(\eta)}{\mathrm{d}\eta}\frac{\partial\phi_1}{\partial\eta} + \frac{\mathrm{d}\varphi_4(\eta)}{\mathrm{d}\eta}\frac{\partial\phi_2}{\partial\eta}, \tag{26}$$

$$\frac{\partial^2\phi}{\partial\eta^2}(\eta) = \frac{\mathrm{d}^2\varphi_1(\eta)}{\mathrm{d}\eta^2}\phi_1 + \frac{\mathrm{d}^2\varphi_2(\eta)}{\mathrm{d}\eta^2}\phi_2 + \frac{\mathrm{d}^2\varphi_3(\eta)}{\mathrm{d}\eta^2}\frac{\partial\phi_1}{\partial\eta} + \frac{\mathrm{d}^2\varphi_4(\eta)}{\mathrm{d}\eta^2}\frac{\partial\phi_2}{\partial\eta}, \tag{27}$$

where $\{\varphi_i(\eta)\}_{i=1}^4$ is the set of basis functions in the physical space. These expressions allow one to compute the values of ϕ, $\partial\phi/\partial\eta$, and $\partial^2\phi/\partial\eta^2$ at any point η in $[\eta_1, \eta_2]$ in terms of four nodal unknowns, i.e. the values of the field variable and its first-order derivatives at the two extremes (also grid points) of the element.

3.1.3 Semi-interior elements

As mentioned earlier, a semi-interior element is defined by two nodes: an interior node and a boundary node. The subscripts 1 and 2 are now replaced with b (b represents a boundary node) and g (g an interior grid node), respectively. Assume that the value of ϕ is given at η_b. The conversion system can be formed as

$$\begin{pmatrix} \phi_b \\ \phi_g \\ \frac{\partial\phi_g}{\partial\eta} \end{pmatrix} = \begin{pmatrix} I_b^{(0)}(\eta_b) & I_g^{(0)}(\eta_b) & \eta_b & 1 \\ I_b^{(0)}(\eta_g) & I_g^{(0)}(\eta_g) & \eta_g & 1 \\ I_b^{(1)}(\eta_g) & I_g^{(1)}(\eta_g) & 1 & 0 \end{pmatrix} \begin{pmatrix} w_b \\ w_g \\ C_1 \\ C_2 \end{pmatrix}. \tag{28}$$

It leads to

$$\phi(\eta) = \varphi_1(\eta)\phi_b + \varphi_2(\eta)\phi_g + \varphi_3(\eta)\frac{\partial \phi_g}{\partial \eta}, \tag{29}$$

$$\frac{\partial \phi}{\partial \eta}(\eta) = \frac{\mathrm{d}\varphi_1(\eta)}{\mathrm{d}\eta}\phi_b + \frac{\mathrm{d}\varphi_2(\eta)}{\mathrm{d}\eta}\phi_g + \frac{\mathrm{d}\varphi_3(\eta)}{\mathrm{d}\eta}\frac{\partial \phi_g}{\partial \eta}, \tag{30}$$

$$\frac{\partial^2 \phi}{\partial \eta^2}(\eta) = \frac{\mathrm{d}^2\varphi_1(\eta)}{\mathrm{d}\eta^2}\phi_b + \frac{\mathrm{d}^2\varphi_2(\eta)}{\mathrm{d}\eta^2}\phi_g + \frac{\mathrm{d}^2\varphi_3(\eta)}{\mathrm{d}\eta^2}\frac{\partial \phi_g}{\partial \eta}. \tag{31}$$

It can be seen that the conversion matrix in (28) is under-determined and its inverse can be obtained using the SVD technique (pseudo-inversion). Owing to the facts that point collocation is used and the RBF conversion matrix is not over-determined, the boundary condition ϕ_b is imposed in an exact manner. For other types of semi-interior elements, the reader is referred to An-Vo, Mai-Duy, and Tran-Cong (2011) for details.

4 Proposed C^2-continuous subregion/point collocation methods

In this study, 2-node IRBFEs are extended to the solution of the stream function-vorticity formulation. In addition, several high-order upwind schemes are incorporated into the 2-node IRBFE methods to enhance their performance for the case of convection-dominant flows. The proposed methods lead to a sparse system and their solution is a C^2 function across IRBFEs.

4.1 Discretisation of governing equations

Two formulations, namely subregion collocation and point collocation, are employed to discretise the governing differential equations. As mentioned earlier, the structure of a steady flow is found through the method of false transients. Time derivative terms in (5) and (6) are simply approximated here with a first-order backward difference.

4.1.1 Subregion collocation

Consider a grid point P surrounded by a rectangular control volume Ω_P (Fig. 3). There are no gaps and overlapping regions between control volumes. For integrals involving the rate of change and generation, the value of the quantity at P is assumed to prevail over Ω_P. Using the middle-point rule to evaluate the integrals of the convection and diffusion terms over Ω_P, equations (9) and (10) become

$$-\frac{A_P}{\Delta t}\psi_P + \left[\left(\frac{\partial \psi}{\partial x}\right)_e \Delta y - \left(\frac{\partial \psi}{\partial x}\right)_w \Delta y + \left(\frac{\partial \psi}{\partial y}\right)_n \Delta x - \left(\frac{\partial \psi}{\partial y}\right)_s \Delta x\right] = -A_P\left(\omega_P^0 + \frac{\psi_P^0}{\Delta t}\right),$$

(32)

$$-\frac{A_P}{\Delta t}\omega_P+\left[\left(\frac{\partial\omega}{\partial x}\right)_e\Delta y-\left(\frac{\partial\omega}{\partial x}\right)_w\Delta y+\left(\frac{\partial\omega}{\partial y}\right)_n\Delta x-\left(\frac{\partial\omega}{\partial y}\right)_s\Delta x\right]$$
$$+Re\left[-\left(\omega\frac{\partial\psi}{\partial y}\right)_e\Delta y+\left(\omega\frac{\partial\psi}{\partial y}\right)_w\Delta y+\left(\omega\frac{\partial\psi}{\partial x}\right)_n\Delta x-\left(\omega\frac{\partial\psi}{\partial x}\right)_s\Delta x\right]=-\frac{A_P}{\Delta t}\omega_P^0, \tag{33}$$

where the superscript 0 represents the value obtained from the previous time level; the subscripts e,w,n and s denote the values of the property at the intersections of grid lines and the east, west, north and south faces of a CV; and A_P the volume of Ω_P. It can be seen that equations (32) and (33) require the estimation of first derivative values of ψ and ω at the interface points e,w,n and s.

4.1.2 Point collocation

Consider a grid point P. Collocating (5) and (6) at P, one obtains

$$-\frac{\psi_P}{\Delta t}+\frac{\partial^2\psi_P}{\partial x^2}+\frac{\partial^2\psi_P}{\partial y^2}=-\left(\omega_P^0+\frac{\psi_P^0}{\Delta t}\right), \tag{34}$$

$$-\frac{\omega_P}{\Delta t}+\frac{\partial^2\omega_P}{\partial x^2}+\frac{\partial^2\omega_P}{\partial y^2}-Re\left(\frac{\partial\psi_P}{\partial y}\frac{\partial\omega_P}{\partial x}-\frac{\partial\psi_P}{\partial x}\frac{\partial\omega_P}{\partial y}\right)=-\frac{\omega_P^0}{\Delta t}. \tag{35}$$

It can be seen that equations (34) and (35) require the estimation of both first and second derivative values of ψ and ω at the collocation point P.

4.2 Approximations of diffusion term

The diffusion term is treated implicitly. Its role is important at regions where the strength of the convection term is small. 2-node IRBFEs are employed here for the approximation of the second terms on the LHSs of (32) and (33) in the subregion collocation framework and (34) and (35) in the point collocation framework. Let E,W,N and S denote the east, west, north and south neighbouring nodes of P, respectively. One can form 4 two-node IRBFEs, namely WP,PE,SP and PN.

4.2.1 Subregion collocation

In the case that WP and PE are interior elements, the values of the flux at $x=x_e$ and $x=x_w$ are computed by using (26)

$$\left(\frac{\partial\phi}{\partial x}\right)_e=\frac{\mathrm{d}\varphi_1(x_e)}{\mathrm{d}x}\phi_P+\frac{\mathrm{d}\varphi_2(x_e)}{\mathrm{d}x}\phi_E+\frac{\mathrm{d}\varphi_3(x_e)}{\mathrm{d}x}\frac{\partial\phi_P}{\partial x}+\frac{\mathrm{d}\varphi_4(x_e)}{\mathrm{d}x}\frac{\partial\phi_E}{\partial x}, \tag{36}$$

$$\left(\frac{\partial\phi}{\partial x}\right)_w=\frac{\mathrm{d}\varphi_1(x_w)}{\mathrm{d}x}\phi_W+\frac{\mathrm{d}\varphi_2(x_w)}{\mathrm{d}x}\phi_P+\frac{\mathrm{d}\varphi_3(x_w)}{\mathrm{d}x}\frac{\partial\phi_W}{\partial x}+\frac{\mathrm{d}\varphi_4(x_w)}{\mathrm{d}x}\frac{\partial\phi_P}{\partial x}, \tag{37}$$

where ϕ represents ψ and ω.

In the case that WP is a semi-interior element, the value of the flux at $x = x_w$ is computed by using (30)

$$\left(\frac{\partial \phi}{\partial x}\right)_w = \frac{\mathrm{d}\varphi_1(x_w)}{\mathrm{d}x}\phi_W + \frac{\mathrm{d}\varphi_2(x_w)}{\mathrm{d}x}\phi_P + \frac{\mathrm{d}\varphi_3(x_w)}{\mathrm{d}x}\frac{\partial \phi_P}{\partial x}. \tag{38}$$

Expressions for the flux at $y = y_n$ and $y = y_s$ are of similar forms.

4.2.2 Point collocation

The values of $\partial^2\psi/\partial x^2$ and $\partial^2\omega/\partial x^2$ at P can be derived from 2-node IRBFEs in the x direction, i.e. WP and PE. It will be shown later that these two elements give the same results, and one can thus choose one of them for calculation, e.g. WP. Through (27) if WP is an interior element and (31) if WP is a semi-interior element, the required values are, respectively, estimated as

$$\frac{\partial^2 \phi_P}{\partial x^2} = \frac{\mathrm{d}^2\varphi_1(x_P)}{\mathrm{d}x^2}\phi_W + \frac{\mathrm{d}^2\varphi_2(x_P)}{\mathrm{d}x^2}\phi_P + \frac{\mathrm{d}^2\varphi_3(x_P)}{\mathrm{d}x^2}\frac{\partial \phi_W}{\partial x} + \frac{\mathrm{d}^2\varphi_4(x_P)}{\mathrm{d}x^2}\frac{\partial \phi_P}{\partial x} \tag{39}$$

and

$$\frac{\partial^2 \phi_P}{\partial x^2} = \frac{\mathrm{d}^2\varphi_1(x_P)}{\mathrm{d}x^2}\phi_W + \frac{\mathrm{d}^2\varphi_2(x_P)}{\mathrm{d}x^2}\phi_P + \frac{\mathrm{d}^2\varphi_3(x_P)}{\mathrm{d}x^2}\frac{\partial \phi_P}{\partial x}, \tag{40}$$

where ϕ represents ψ and ω.

The values of $\partial^2\psi/\partial y^2$ and $\partial^2\omega/\partial y^2$ at P can be computed in a similar fashion.

4.3 Approximations of convection term

At high values of the *Re* number, the third term (i.e. convection term) on the LHS of (33) or (35) is dominant and strongly affects the stability of a numerical solution. From a physical point of view, convection is directed by the velocity field from the upstream to the downstream of the flow. Three high-order upwind schemes, namely Scheme 1, Scheme 2 and Scheme 3, are proposed here for the discretisation of the convection term.

4.3.1 Scheme 1 for subregion collocation

This scheme is concerned with an upwind treatment with the deferred correction strategy. Let f be the intersection of the CV face and the grid line. The value of ω at point f is computed as

$$\omega_f = \omega_U + \Delta\omega_f, \tag{41}$$

where ω_U is the upstream value and $\Delta\omega_f$ the correction term that is a known value. It is noted that f represents w, e, s and n. $\Delta\omega_f$ is presently derived from the 2-node IRBFE approximation, i.e. (25) and (29). As an example, when $f \equiv w$ and $u_w > 0$, one has

$$\omega_U = \omega_W, \tag{42}$$

$$\Delta\omega_f = (\varphi_1(x_w) - 1)\omega_W^0 + \varphi_2(x_w)\omega_P^0 + \varphi_3(x_w)\frac{\partial \omega_W^0}{\partial x} + \varphi_4(x_w)\frac{\partial \omega_P^0}{\partial x}, \tag{43}$$

where the superscript 0 is used to denote the values obtained from the previous time level. For a special case, where W is a boundary point, expression (43) reduces to

$$\Delta\omega_f = (\varphi_1(x_w) - 1)\omega_W^0 + \varphi_2(x_w)\omega_P^0 + \varphi_3(x_w)\frac{\partial \omega_P^0}{\partial x}. \tag{44}$$

When the solution reaches a steady state, ω_fs are purely predicted by 2-node IRBFEs and their accuracy is thus recovered. Velocity values in the convection term are simply estimated by a linear profile

$$\left(\frac{\partial \psi}{\partial y}\right)_e = \frac{1}{2}\left(\frac{\partial \psi_P^0}{\partial y} + \frac{\partial \psi_E^0}{\partial y}\right), \tag{45}$$

$$\left(\frac{\partial \psi}{\partial y}\right)_w = \frac{1}{2}\left(\frac{\partial \psi_W^0}{\partial y} + \frac{\partial \psi_P^0}{\partial y}\right), \tag{46}$$

$$\left(\frac{\partial \psi}{\partial x}\right)_n = \frac{1}{2}\left(\frac{\partial \psi_P^0}{\partial x} + \frac{\partial \psi_N^0}{\partial x}\right), \tag{47}$$

$$\left(\frac{\partial \psi}{\partial x}\right)_s = \frac{1}{2}\left(\frac{\partial \psi_S^0}{\partial x} + \frac{\partial \psi_P^0}{\partial x}\right). \tag{48}$$

4.3.2 Scheme 2 for point collocation

Without loss of generality, assuming that $u_P > 0$. W thus becomes an upstream node. A special approximation is constructed over WP for the purpose of computing $\partial\omega_P/\partial x$; not only ω_W and $\partial\omega_W/\partial x$ but also $\partial^2\omega_W/\partial x^2$ are employed in the conversion process

$$\begin{pmatrix} \omega_P \\ \omega_W \\ \frac{\partial \omega_W}{\partial \eta} \\ \frac{\partial^2 \omega_W}{\partial \eta^2} \end{pmatrix} = \begin{pmatrix} I_1^{(0)}(x_P) & I_2^{(0)}(x_P) & x_P & 1 \\ I_1^{(0)}(x_W) & I_2^{(0)}(x_W) & x_W & 1 \\ I_1^{(1)}(x_W) & I_2^{(1)}(x_W) & 1 & 0 \\ I_1^{(2)}(x_W) & I_2^{(2)}(x_W) & 0 & 0 \end{pmatrix} \begin{pmatrix} w_1 \\ w_2 \\ C_1 \\ C_2 \end{pmatrix}. \tag{49}$$

This leads to

$$\frac{\partial \omega_P}{\partial x} = \frac{\mathrm{d}\varphi_1(x_P)}{\mathrm{d}x}\omega_P + \frac{\mathrm{d}\varphi_2(x_P)}{\mathrm{d}x}\omega_W + \frac{\mathrm{d}\varphi_3(x_P)}{\mathrm{d}x}\frac{\partial \omega_W}{\partial x} + \frac{\mathrm{d}\varphi_4(x_P)}{\mathrm{d}x}\frac{\partial^2 \omega_W}{\partial x^2}. \tag{50}$$

4.3.3 Scheme 3 for point collocation

Assuming that $u_P > 0$. W becomes an upstream point. The value of $\partial\omega/\partial x$ at P is estimated over WP with the deferred correction strategy

$$\frac{\partial\omega_P}{\partial x} = \left(\frac{\omega_P - \omega_W}{h}\right) + \Delta\left(\frac{\partial\omega_P}{\partial x}\right), \tag{51}$$

where h is the length of WP, the first term on the RHS is simply a standard linear estimation; and the second term is a correction amount defined as

$$\Delta\left(\frac{\partial\omega_P}{\partial x}\right) = -\left(\frac{\omega_P^0 - \omega_W^0}{h}\right) + \left(\frac{\partial\omega_P}{\partial x}\right)^0, \tag{52}$$

The value $(\partial\omega_P/\partial x)^0$ in (52) is obtained using (26) if WP is an interior element and using (30) if WP is a semi-interior element. When the flow is steady, the first term on the RHS of (51) and the first term on the RHS of (52) will cancel out each other.

4.4 C^2 continuity solution

It can be seen from IRBFE expressions for computing the flux ($\partial\phi/\partial x$ or $\partial\phi/\partial y$) at the CV faces (e.g. (36), (37)) and $\partial^2\phi/\partial x^2$ and $\partial^2\phi/\partial y^2$ at a nodal point P, e.g. (39), there are three unknowns, namely ϕ, $\partial\phi/\partial x$ and $\partial\phi/\partial y$, at a nodal point P. It is noted that ϕ represents ψ and ω. Unlike conventional subregion/point collocation methods, the nodal values of $\partial\phi/\partial x$ and $\partial\phi/\partial y$ at P here constitute part of the nodal unknown vector. One thus needs to generate three independent equations. The first equation is obtained by conducting subregion/point collocation at P, i.e. (32)-(33) or (34)-(35), respectively. The other two equations can be formed by enforcing the local continuity of $\partial^2\phi/\partial x^2$ and $\partial^2\phi/\partial y^2$ across the elements at P

$$\left(\frac{\partial^2\phi_P}{\partial x^2}\right)_L = \left(\frac{\partial^2\phi_P}{\partial x^2}\right)_R, \tag{53}$$

$$\left(\frac{\partial^2\phi_P}{\partial y^2}\right)_B = \left(\frac{\partial^2\phi_P}{\partial y^2}\right)_T, \tag{54}$$

where $(.)_L$ indicates that the computation of $(.)$ is based on the element to the left of P, i.e. element WP, and similarly subscripts R,B,T denote the right *(PE)*, bottom *(SP)* and top *(PN)* elements.

Substitution of (24) into (53) and (54) yields

$$\left(\left[I_1^{(2)}(\eta_2), I_2^{(2)}(\eta_2), 0, 0\right]\mathscr{I}^{-1}\widehat{\phi}\right)_L = \left(\left[I_1^{(2)}(\eta_1), I_2^{(2)}(\eta_1), 0, 0\right]\mathscr{I}^{-1}\widehat{\phi}\right)_R, \tag{55}$$

where η represents x and $\eta_2 \equiv \eta_1 \equiv x_P$, and

$$\left(\left[I_1^{(2)}(\eta_2), I_2^{(2)}(\eta_2), 0, 0\right] \mathscr{I}^{-1}\widehat{\phi}\right)_B = \left(\left[I_1^{(2)}(\eta_1), I_2^{(2)}(\eta_1), 0, 0\right] \mathscr{I}^{-1}\widehat{\phi}\right)_T, \qquad (56)$$

where η represents y and $\eta_2 \equiv \eta_1 \equiv y_P$. The conditions (53)-(54) or (55)-(56) guarantee that the solution ϕ across IRBFEs is a C^2 function.

Collection of the governing equations and the continuity equations at the interior grid points leads to a square system of algebraic equations. Since local approximations are presently based on two RBFs only, the resultant system matrix is sparse and a wide range of β can be used. One can thus control the solution accuracy by means of the number of RBFs and/or the shape parameter. It can be seen that two-point line elements are well suited to discretisation methods based on Cartesian grids.

5 Numerical examples

The performance of the proposed C^2 discretisation methods with three upwind schemes, i.e. Scheme 1, Scheme 2 and Scheme 3, is studied through the simulation of lid-driven cavity flows and flows past a circular cylinder in a channel. The subregion collocation version is from now on denoted by IRBFE-CVM while IRBFE-CM is used to represent the point collocation version. For all numerical examples presented in this study, the MQ shape parameter a is simply chosen proportionally to the element length h by a factor β. The effects of the shape parameter on the solution accuracy is thus investigated through the parameter β. In the case of non-rectangular domains, there may be some nodes that are too close to the boundary. If an interior node falls within a distance of $h/2$ to the boundary, such a node is removed from the set of nodal points. A steady solution is obtained with a time marching approach starting from a computed solution at a lower Reynolds number. For the special case of Stokes equation, the starting condition is the rest state.

The solution procedure involves the following steps
(1) Guess the initial distributions of the stream function and vorticity in the case of Stokes flow. Otherwise, take the solution of a lower Reynolds number as an initial guess.
(2) Solve the stream-function equation (32)/(34) subject to Dirichlet boundary conditions, and calculate the nonlinear terms in the vorticity equation (33)/(35) by the upwind schemes.
(3) Estimate Dirichlet boundary conditions for the vorticity equation (33)/(35) from the Neumann boundary conditions of the stream function.
(4) Solve the vorticity equation (33)/(35).
(5) Check to see whether the solution has reached a steady state through a condition

on convergence measure

$$CM(\psi) = \frac{\sqrt{\sum_{i=1}^{N} (\psi_i - \psi_i^0)^2}}{\sqrt{\sum_{i=1}^{N} \psi_i^2}} < 10^{-9}, \tag{57}$$

where N is the total number of grid nodes.
(6) If CM is not satisfactorily small, advance pseudo-time and repeat from step (2). Otherwise, stop the computation and output the results.

5.1 Lid-driven cavity flow

Lid-driven cavity flow is a very useful benchmark problem for the validation of new numerical methods in CFD because of its simple geometry and rich flow physics at different Reynolds numbers. The cavity is taken to be a unit square, with the lid sliding from left to right at a unit velocity. The boundary conditions for u and v become

$$\begin{array}{llll} \psi = 0, & \partial\psi/\partial x = 0, & x = 0, & x = 1, \\ \psi = 0, & \partial\psi/\partial y = 0, & y = 0, & \\ \psi = 0, & \partial\psi/\partial y = 1, & y = 1. & \end{array}$$

Both IRBFE-CVM and IRBFE-CM are considered here. We take Dirichlet boundary conditions, $\psi = 0$, on all walls for solving (32) and (34). The Neumann boundary conditions, $\partial\psi/\partial n$ (i.e. $\partial\psi/\partial n = \nabla\psi \cdot \hat{n}$, where $\hat{n}$ is the outward unit normal vector at a point on the boundary), are used to derive computational boundary conditions for ω in solving (33) and (35). Making use of (1), the values of ω on the boundaries are computed by

$$\omega_b = -\frac{\partial^2\psi_b}{\partial x^2}, \qquad x = 0 \text{ and } x = 1, \tag{58}$$

$$\omega_b = -\frac{\partial^2\psi_b}{\partial y^2}, \qquad y = 0 \text{ and } y = 1. \tag{59}$$

In computing (58) and (59), one needs to incorporate $\partial\psi_b/\partial x$ into $\partial^2\psi_b/\partial x^2$, and $\partial\psi_b/\partial y$ into $\partial^2\psi_b/\partial y^2$, respectively. We present a simple technique to derive boundary values for ω in the context of 2-node IRBFEs. Assuming that node 1 and 2 of an IRBFE are a boundary node and an interior grid node respectively (i.e. $1 \equiv b$ and $2 \equiv g$). Boundary values of the vorticity are obtained by applying (27) as

$$\omega_b = -\frac{\partial^2\psi_b}{\partial\eta^2} = -\left(\frac{\mathrm{d}^2\varphi_1(\eta_b)}{\mathrm{d}\eta^2}\psi_b + \frac{\mathrm{d}^2\varphi_2(\eta_b)}{\mathrm{d}\eta^2}\psi_g + \frac{\mathrm{d}^2\varphi_3(\eta_b)}{\mathrm{d}\eta^2}\frac{\partial\psi_b}{\partial\eta} + \frac{\mathrm{d}^2\varphi_4(\eta_b)}{\mathrm{d}\eta^2}\frac{\partial\psi_g}{\partial\eta}\right), \tag{60}$$

where η represents x and y; ψ_b and $\partial\psi_b/\partial\eta$ are the Dirichlet and Neumann boundary conditions for ψ, and ψ_g and $\partial\psi_g/\partial\eta$ are known values taken from the solution of the stream-function equation (32)/(34). It is noted that (i) all given boundary conditions are imposed in an exact manner; and (ii) this technique only requires the local values of ψ and $\partial\psi/\partial\eta$ at the boundary node and its adjacent grid node to estimate the Dirichlet boundary conditions for the vorticity equation (33)/(35).

It can be seen that the set of 2-node IRBFEs is generated here from grid lines that pass through interior grid nodes. As a result, the set of interpolation points does not include the four corners of the cavity and hence corner singularities do not explicitly enter the discrete system.

Simulation is carried out for a wide range of *Re*, namely (100, 400, 1000, 3200). Grid convergence is studied using 12 uniform grids, i.e. (11×11, 21×21, ..., 121×121). Results obtained are compared with the benchmark solutions taken from Ghia, Ghia, and Shin (1982) and Botella and Peyret (1998) to assess the performance of the present methods. The former was obtained using a multi-grid based finite-difference method with fine grids. For the latter, spectral scheme and analytical method were employed to calculate the regular and singular parts of the solution and the benchmark results were given for $Re = 100$ and $Re = 1000$. In addition, global 1D-IRBF subregion/point collocation (1D-IRBF-CVM/CM) results and also standard CV results, recently given in Mai-Duy and Tran-Cong (2009, 2010), are also included. It is noted that, in Mai-Duy and Tran-Cong (2010), CD-CD means that both the convection and diffusion terms were approximated with a central difference, while UW-CD means that the convection term is treated with a first-order upwind.

Time-step convergence: The convergence behaviours of IRBFE-CVM and IRBFE-CM with respect to time are shown in Figs 4, 5 and 6. Results without an upwind treatment are also presented. It can be seen that solutions converge remarkably faster for those with upwind than those without upwind. Much larger time steps can be used for the former. Consider the case of $Re = 1000$ and a grid of 81×81 (Figs 4 and 5). IRBFE-CVM reaches $CM < 10^{-9}$ after about 5×10^4 iterations for its no-upwind version and after about 2.5×10^3 iterations for Scheme 1, while IRBFE-CM requires about 6.9×10^4 for its no-upwind version and about 2.5×10^3 for Scheme 2, 6.8×10^3 for Scheme 3. It was reported in Mai-Duy and Tran-Cong (2010) that the global 1D-IRBF-CVM takes about 8.5×10^4 and 1.2×10^4 iterations to have $CM < 10^{-8}$ for its no-upwind and upwind versions, respectively. It appears that local IRBF versions help make the convergence faster. In the case of $Re = 3200$ and a grid of 91×91, in contrast to the upwind version, the no-upwind version is not able to reach $CM = 10^{-9}$ as shown in Fig. 6.

Grid-size convergence: The convergence of velocity profiles on the vertical and horizontal centrelines at $Re = (0, 100, 400, 1000, 3200)$ with respect to grid refinement is presented in Figs 7 and 8 and Tabs 1-4. Benchmark results by Ghia, Ghia, and Shin (1982) and Botella and Peyret (1998) are also included for comparison purposes. It can be seen that (i) errors relative to the benchmark results are consistency reduced as the grid is refined; and (ii) converged profiles are obtained with relatively coarse grids (e.g. 21×21 for $Re = 100$ and 61×61 for $Re = 1000$).

Solution quality: The solution qualities of IRBFE-CVM and IRBFE-CM are shown in Tabs 1-4 and Figs 9-10. Tabs 1-4 reveal that the present results are closer to the benchmark spectral solutions than the benchmark finite-difference results and also those of the global 1D-IRBF-CVM. Errors relative to the benchmark spectral results are less than 1% for $Re = 100$ using a grid of 41×41 (Tab. 1) and for $Re = 1000$ using a grid of 91×91 (Tab. 3). These IRBFE results correspond to $\beta = 15$. Tab. 4 indicates that the solution accuracy can be controlled by means of β. The quality of the solution can be significantly improved at the optimal value of β. It can be seen from Figs 9-10 that smooth contours are obtained for both the stream function and vorticity fields and the corner eddies are clearly captured at relatively coarse grids.

5.2 Flow past a circular cylinder in a channel

We further verify IRFBE-CVM and IRBFE-CM through the simulation of flow past a circular cylinder in a channel (Fig. 11). Works involving simulation of such a flow are reported in, for example, Chen, Pritchard, and Tavener (1995), Sahin and Owens (2004) and Singha and Sinhamahapatra (2010). Let D be the cylinder diameter and H the channel height. One important geometric parameter to characterise the flow is the blockage ratio defined as $\gamma = D/H$. Chen, Pritchard, and Tavener (1995) did a numerical linear stability analysis and identified the curve of neutral stability for Hopf bifurcation at values of γ up to 0.7. Sahin and Owens (2004) extended the linear stability analysis to a wider range of γ from 0.1 to 0.9 and uncovered the complex dynamics of the flow at sufficiently high values of the Reynolds number and the blockage ratio. The paper by Anagnostopoulos and Iliadis (1996) provided the flow patterns for $\gamma = (0.05, 0.15, 0.25)$ and $Re = 106$ using the finite element technique. Recently, Singha and Sinhamahapatra (2010) reported the flow patterns for $Re = (45, 100, 150)$ and $\gamma = (0.5, 0.25, 0.333, 0.125)$ using the finite volume technique.

The problem domain is multiply-connected as shown in Fig. 11. We choose the geometry and boundary conditions here as those in Chen, Pritchard, and Tavener (1995). The ratio between the upstream and downstream lengths is taken to be $1/3$ and the length of the channel is chosen to be $6H$ to assure the fully developed

conditions of the flow at upstream and downstream boundaries (Chen, Pritchard, and Tavener (1995)). All lengths are scaled by the channel height H (Fig. 11). Parabolic velocity profiles can thus be imposed at the inlet and outlet as

$$u_{in} = u_{out} = u_0 \left(\frac{1}{4} - y^2 \right), \tag{61}$$

$$v_{in} = v_{out} = 0. \tag{62}$$

Using $u_0 = 1$, the flow rate takes the value

$$Q = \int_{-1/2}^{1/2} \left(\frac{1}{4} - y^2 \right) \mathrm{d}y = \frac{1}{6}, \tag{63}$$

and we define the Reynolds number as $Re = 1/(6\nu)$. Fig. 11 displays boundary conditions for the stream function variable, which are derived from (61)-(62) at the inlet and outlet, and non-slip conditions at the remaining boundaries. The imposition of boundary conditions for ω on the walls, inlet and outlet are similar to that used in the lid driven-cavity flow, i.e. (60). On the cylinder surface, analytic formulae for computing the vorticity boundary condition on a non-rectangular boundary Le-Cao, Mai-Duy, and Tran-Cong (2009) are utilised here

$$\omega_b = -\left[1 + \left(\frac{t_x}{t_y} \right)^2 \right] \frac{\partial^2 \psi_b}{\partial x^2}, \tag{64}$$

for an x-grid line, and

$$\omega_b = -\left[1 + \left(\frac{t_y}{t_x} \right)^2 \right] \frac{\partial^2 \psi_b}{\partial y^2}, \tag{65}$$

for a y-grid line. In (64) and (65), t_x and t_y are the x- and y-components of the unit vector tangential to the boundary. The approximations in (64) and (65) require information about ψ in one direction only and they are conducted here by means of 2-node IRBFEs, i.e. (27).

We implement Scheme 1 of IRBFE-CVM and Scheme 3 of IRBFE-CM with three different grids, $(127 \times 22, 247 \times 42, 367 \times 62)$, to study the flow at $Re = (0, 25, 35, 60)$ and $\gamma = (0.3, 0.5, 0.7)$.

The convergence behaviours of IRBFE-CVM and IRBFE-CM with respect to time in the case of $\gamma = 0.5$, $Re = 60$ and a grid of 367×62 are shown in Figs 12 and 13. Results without an upwind treatment are also included. It can be seen that solutions converge faster for those with upwind than those without upwind. Larger time steps can be used for the former. In the case of IRBFE-CVM (Fig. 12), $CM = 10^{-9}$ is

obtained after about 3.3×10^3 iterations for the no-upwind version and after about 1.8×10^3 iterations for Scheme 1. In Fig. 13, IRBFE-CM reaches $CM = 10^{-9}$ after about 1.7×10^4 iterations for the no-upwind version and after about 8.3×10^3 iterations for Scheme 3.

Results concerning the critical *Re* number and the length of recirculation zones behind the cylinder are shown in Tabs 5 and 6, respectively. For all three grids and different values of β used, the obtained values are in satisfactory agreement with those reported in Chen, Pritchard, and Tavener (1995) and Singha and Sinhamahapatra (2010).

Contour plots for the stream function and vorticity fields are presented in Figs 14, 15 and 16, while the velocity vector field is displayed in Fig. 17. Stronger interaction in regions between the cylinder and the walls is observed at higher values of the blockage ratio (Figs 14 and 15). At $Re = 60$ and $\gamma = 0.5$, symmetrical recirculation zones appear behind the cylinder in the stream function field (Fig. 16a). The flow features are similar to those obtained by Singha and Sinhamahapatra (2010) at $Re = 45$ (i.e. $Re = 60$ according to the present definition of *Re*) and $\gamma = 0.5$. Fig. 18 shows velocity profiles on the centreline behind the cylinder for the case of $\gamma = 0.5$. It can be seen that the incipience of recirculation zones appears around $Re = 25$.

6 Concluding remarks

In this paper, we have extended our 2-node IRBFEs to the solution of the stream function-vorticity formulation governing fluid flows in rectangular and non-rectangular domains. Several high-order upwind schemes based on 2-node IRBFEs were also proposed and investigated. Attractive features of the proposed point/subregion collocation methods include (i) a simple preprocessing (Cartesian grids); (ii) a sparse system matrix (2-node approximations); and a higher order of continuity across grid nodes (C^2-continuous elements). Numerical results show that (i) much larger time steps can be used with the upwind versions; and (ii) a high level of accuracy is achieved using relatively coarse grids.

Acknowledgement: D.-A. An-Vo would like to thank USQ, FoES and CESRC for a PhD scholarship. This work was supported by the Australian Research Council.

References

An-Vo, D.-A.; Mai-Duy, N.; Tran-Cong, T. (2011): A C^2-continuous control-volume technique based on Cartesian grids and two-node integrated-RBF elements

for second-order elliptic problems. *CMES: Computer Modeling in Engineering and Sciences*, vol. 72 (4), pp. 299–334.

Anagnostopoulos, P.; Iliadis, G. (1996): Numerical study of the blockage effects on viscous flow past a circular cylinder. *International Journal for Numerical Methods in Fluids*, vol. 22, pp. 1061–1074.

Atluri, S. N.; Shen, S. (2002): *The meshless local Petrov-Galerkin (MLPG) method*. Tech Science Press.

Botella, O.; Peyret, R. (1998): Benchmark spectral results on the lid-driven cavity flow. *Computers & Fluids*, vol. vol. 27, pp. 421–433.

Chen, C. S.; Karageorghis, A.; Smyrlis, Y. S. (2008): *The method of fundamental solutions - A meshless method*. Dynamic Publishers.

Chen, J. H.; Pritchard, W. G.; Tavener, S. J. (1995): Bifurcation for flow past a cylinder between parallel planes. *Journal of Fluid Mechanics*, vol. 284, pp. 23–41.

Cheng, A. H. D.; Golberg, M. A.; Kansa, E. J.; Zammito, G. (2003): Exponential convergence and h-c multiquadric collocation method for partial differential equations. *Numerical Methods for Partial Differential Equations*, vol. 19, pp. 571–594.

Courant, R.; Isaccson, E.; Rees, M. (1952): On the solution of non-linear hyperbolic differential equations by finite differences. *Communications on Pure and Applied Mathematics*, vol. 5, pp. 243.

Divo, E.; Kassab, A. (2007): An efficient localized radial basis function meshless method for fluid flow and conjugate heat transfer. *Journal of Heat Transfer*, vol. vol. 129, pp. 124–136.

Fasshauer, G. E. (2007): *Meshfree approximation methods with Matlab*. Interdisciplinary mathematical sciences, vol. 6. Singapore: World Scientific Publishers.

Gentry, R. A.; Martin, R. E.; Daly, B. J. (1966): An Eulerian differencing method for unsteady compressible flow problems. *Journal of Computational Physics*, vol. 1, pp. 87–118.

Ghia, U.; Ghia, K. N.; Shin, C. (1982): High-Re Solutions for Incompressible Flow Using the Navier-Stokes equations and a Multigrid method. *Journal of Computational Physics*, vol. vol. 48, pp. 387–411.

Huang, C.-S.; Lee, C.-F.; Cheng, A.-D. (2007): Error estimate, optimal shape factor, and high precision computation of multiquadric collocation method. *Engineering Analysis with Boundary Elements*, vol. 31, pp. 614–623.

Huang, J.; Greengard, L. (2000): A fast direct solver for elliptic partial differential equations on adaptively refined meshes. *SIAM Journal on Scientific Computing*, vol. 21, pp. 1551–1566.

Huilgol, R.; Phan-Thien, N. (1997): *Fluid mechanics of viscoelasticity*. Elsevier: Amsterdam.

Kansa, E. (1990): Multiquadrics-a scattered data approximation scheme with applications to computational fluid-dynamics-II. *Computers & Mathematics with Applications*, vol. vol. 19, pp. 147–161.

Khosla, P. K.; Rubin, S. G. (1974): A diagonally dominant second-order accurate implicit scheme. *Computers and Fluids*, vol. 2 (2), pp. 207–209.

Le-Cao, K.; Mai-Duy, N.; Tran-Cong, T. (2009): An effective intergrated-RBFN Cartesian-grid discretization for the stream function-vorticity-temperature formulation in nonrectangular domains. *Numerical Heat Transfer, Part B: Fundamentals*, vol. 55, pp. 480 – 502.

Leonard, B. P. (1979): A stable and accurate convective modelling procedure based on quadratic upstream interpolation. *Computer Methods in Applied Mechanics and Engineering*, vol. 19, pp. 59–98.

Mai-Duy, N.; Tanner, R. (2005): Solving high order partial differential equations with indirect radial basis function networks. *International Journal for Numerical Method in Engineering*, vol. vol. 63, pp. 1636–1654.

Mai-Duy, N.; Tran-Cong, T. (2001): Numerical solution of differential euqations using multiquadric radial basis function networks. *Neural Networks*, vol. vol. 14, pp. 185–199.

Mai-Duy, N.; Tran-Cong, T. (2003): Approximation of function and its derivatives using radial basis function network methods. *Applied Mathematical Modelling*, vol. vol. 27, pp. 197–220.

Mai-Duy, N.; Tran-Cong, T. (2005): An effective indirect RBFN-based method for numerical solution of PDEs. *Numerical Methods for Partial Differential Equations*, vol. vol. 21, pp. 770–790.

Mai-Duy, N.; Tran-Cong, T. (2009): Integrated radial-basis-function networks for computing Newtonian and non-Newtonian fluid flows. *Computers & Structures*, vol. vol. 87, pp. 642–650.

Mai-Duy, N.; Tran-Cong, T. (2010): A high-order upwind control-volume method based on integrated RBFs for fluid-flow problems. *International Journal for Numerical Methods in Fluids*, vol. 2, pp. 1.

Mallinson, G. D.; Davis, G. D. V. (1973): The method of the false transient for the solution of coupled elliptic equations. *Journal of Computational Physics*, vol. 12, pp. 435–461.

Patankar, S. (1980): *Numerical heat transfer and fluid flow*. Taylor & Francis.

Patankar, S. V. (1981): A calculation procedure for two-dimensional elliptic situations. *Numerical Heat Transfer, Part B*, vol. 4, pp. 409–425.

Pozrikidis, C. (1997): *Introduction to theoretical and computational fluid dynamics*. Oxford University Press.

Sahin, M.; Owens, R. G. (2003): A novel fully implicit finite volume method applied to the lid-driven cavity problem - Part I: High Reynolds number flow calculations. *International Journal for Numerical Method in Fluids*, vol. vol. 42, pp. 57–77.

Sahin, M.; Owens, R. G. (2004): A numerical investigation of wall effects up to high blockage ratios on two-dimensional flow past a confined circular cylinder. *Physics of Fluids*, vol. 16, pp. 1305–1320.

Shu, C.; Ding, H.; Yeo, K. (2003): Local radial basis function-based differential quadrature method and its application to solve two-dimensional incompressible Navier-Stokes equations. *Computer Methods in Applied Mechanics & Engineering*, vol. vol. 192, pp. 941–954.

Singha, S.; Sinhamahapatra, K. P. (2010): Flow past a circular cylinder between parallel walls at low Reynolds numbers. *Ocean Engineering*, vol. 37, pp. 757–769.

Spalding, D. B. (1972): A novel finite-difference formulation for differential expression involving both first and second derivatives. *International Journal for Numerical Method in Engineering*, vol. 4, pp. 551–559.

Šarler, B.; Vertnik, R. (2006): Meshfree explicit local radial basis function collocation method for diffusion problems. *Computer & Mathematics with Applications*, vol. vol. 51, pp. 1269–1282.

Table 1: Lid-driven cavity flow, IRBFE-CVM, $Re = 100$: extrema of velocity profiles on the vertical and horizontal centre-lines of the cavity. [$\star$] is Ghia, Ghia, and Shin (1982) and [$\star\star$] is Botella and Peyret (1998).

Method	Grid	u_{min}	Error %	y	v_{max}	Error %	x	v_{min}	Error %	x
IRBFE-CVM	11x11	-0.20604	3.74	0.505	0.15971	11.06	0.225	-0.21745	14.32	0.804
	21x21	-0.21190	1.00	0.466	0.17609	1.94	0.235	-0.24673	2.79	0.809
	31x31	-0.21288	0.55	0.462	0.17798	0.89	0.236	-0.25077	1.20	0.810
	41x41	-0.21327	0.36	0.460	0.17857	0.56	0.237	-0.25203	0.70	0.810
FDM ($\psi - \omega$) [$\star$]	129x129	-0.21090	1.47	0.453	0.17527	2.40	0.234	-0.24533	3.34	0.805
Benchmark [$\star\star$]		-0.21404		0.458	0.17957		0.237	-0.25380		0.810

Table 2: Lid-driven cavity flow, IRBFE-CVM, $Re = 1000$: extrema of the vertical and horizontal velocity profiles through the centrelines of the cavity. $[\star]$ is Ghia, Ghia, and Shin (1982) and $[\star\star]$ is Botella and Peyret (1998).

Method	Grid	u_{min}	y	v_{max}	x	v_{min}	x
IRBFE-CVM	31x31	-0.36093	0.195	0.35084	0.167	-0.48074	0.899
	41x41	-0.37140	0.182	0.36144	0.162	-0.50172	0.905
	51x51	-0.37720	0.177	0.36673	0.160	-0.51083	0.907
	61x61	-0.38057	0.176	0.36980	0.160	-0.51588	0.908
	71x71	-0.38266	0.174	0.37166	0.159	-0.51897	0.908
	81x81	-0.38407	0.174	0.37293	0.159	-0.52097	0.909
	91x91	-0.38502	0.173	0.37377	0.159	-0.52233	0.909
	101x101	-0.38569	0.173	0.37437	0.158	-0.52330	0.909
	111x111	-0.38619	0.173	0.37482	0.158	-0.52402	0.909
	121x121	-0.38657	0.172	0.37515	0.158	-0.52454	0.909
FDM $(\psi - \omega)$ $[\star]$	129x129	-0.38289	0.172	0.37095	0.156	-0.51550	0.906
Benchmark $[\star\star]$		-0.38857	0.172	0.37694	0.158	-0.52708	0.909

Table 3: Lid-driven cavity flow, IRBFE-CVM, $Re = 1000$: percentage errors relative to the spectral benchmark results for the extreme values of the velocity profiles on the centrelines. Results of upwind central difference (UW-CD), central difference (CD-CD) and global 1D-IRBF-CVM are taken from Mai-Duy and Tran-Cong (2010).

	Error (%)			
Grid	UW-CD	CD-CD	1D-IRBF-CVM	IRBFE-CVM
			u_{min}	
31x31	46.10	29.19	11.86	7.11
41x41	38.17	18.13	6.50	4.42
51x51	32.92	12.11	4.09	2.93
61x61	29.12	8.63	2.80	2.06
71x71	26.21	6.46	2.03	1.52
81x81	23.88	5.02	1.54	1.16
91x91	21.95	4.01	1.19	0.91
101x101	20.33	3.28	0.96	0.74
111x111	18.94	2.73	0.78	0.61
121x121	17.74	2.31	0.65	0.51
			v_{max}	
31x31	48.01	29.98	11.91	6.92
41x41	39.71	18.45	6.55	4.11
51x51	34.43	12.32	4.13	2.71
61x61	30.62	8.79	2.83	1.90
71x71	27.68	6.58	2.05	1.40
81x81	25.31	5.12	1.56	1.06
91x91	23.34	4.09	1.21	0.84
101x101	21.67	3.35	0.97	0.68
111x111	20.23	2.79	0.79	0.56
121x121	18.98	2.36	0.66	0.48
			v_{min}	
31x31	40.12	29.83	11.53	8.79
41x41	30.42	18.08	6.25	4.81
51x51	24.70	11.90	3.87	3.08
61x61	20.94	8.40	2.58	2.12
71x71	18.24	6.25	1.85	1.54
81x81	16.19	4.83	1.39	1.16
91x91	14.56	3.85	1.07	0.90
101x101	13.24	3.14	0.85	0.72
111x111	12.14	2.61	0.70	0.58
121x121	11.22	2.20	0.58	0.48

Table 4: Lid-driven cavity flow, IRBFE-CM, $Re = 1000$: effects of β on the solution accuracy. The present results at the "optimal" value (i.e. about 3) with a grid of 51×51 are in better agreement with the benchmark spectral results than those by 1D-IRBF-CM using the same grid and by FDM using a much denser grid. $[\star]$ is Mai-Duy and Tran-Cong (2009), $[\star\star]$ is Ghia, Ghia, and Shin (1982), and $[\star\star\star]$ is Botella and Peyret (1998).

Method	Grid	β	u_{min}	Error %	y	v_{max}	Error %	x	v_{min}	Error %	x
IRBFE-CM	51x51	1	-0.36134	7.00	0.188	0.35048	7.02	0.168	-0.48532	7.92	0.898
	51x51	3	-0.38803	0.14	0.174	0.37677	0.05	0.161	-0.52184	0.99	0.906
	51x51	5	-0.38948	0.23	0.174	0.37832	0.37	0.161	-0.52357	0.67	0.906
1D-IRBF-CM $[\star]$	51x51		-0.37985	2.25	0.174	0.36781	2.42	0.160	-0.51469	2.35	0.908
FDM $(\psi - \omega)$ $[\star\star]$	129x129		-0.38289	1.46	0.172	0.37095	1.59	0.156	-0.51550	2.20	0.906
Benchmark $[\star\star\star]$			-0.38857		0.172	0.37694		0.158	-0.52708		0.909

Table 5: Flow past a circular cylinder in a channel, IRBFE-CVM, $\gamma = 0.5$: The critical Reynolds number Re_{crit} for the formation of the steady recirculation zone behind the cylinder.

Method	Grid	Re_{crit}
IRBFE-CVM	127x22	27.498
	247x42	26.133
	367x62	25.078
Chen, Pritchard, and Tavener (1995)		24.3

Table 6: Flow past a circular cylinder in a channel, $\gamma = 0.5$, $Re = 60$: minimum velocity u_{min} and its position on the centreline, and the length of recirculation zones behind the cylinder (L_w). It is noted that the case of $Re = 60$ and $\gamma = 0.5$ here is equivalent to the case of $Re = 45$ and $\gamma = 0.5$ in Singha and Sinhamahapatra (2010).

Method	Grid	β	u_{min}	x	L_w
IRBFE-CVM	127x22	15	-0.067	0.141	0.269
	247x42	15	-0.074	0.140	0.270
	367x62	15	-0.076	0.139	0.270
IRBFE-CM	367x62	1	-0.076	0.141	0.271
	367x62	3	-0.076	0.141	0.270
	367x62	5	-0.075	0.140	0.269
Singha and Sinhamahapatra (2010) ($Re = 45$)					0.284

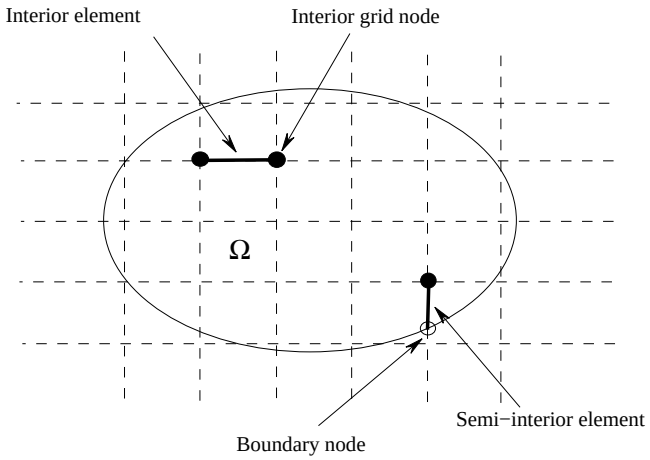

Figure 1: A domain is embedded in a Cartesian grid with interior and semi-interior elements.

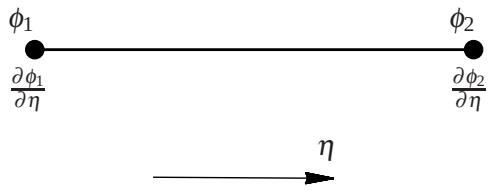

Figure 2: Schematic outline for 2-node IRBFE.

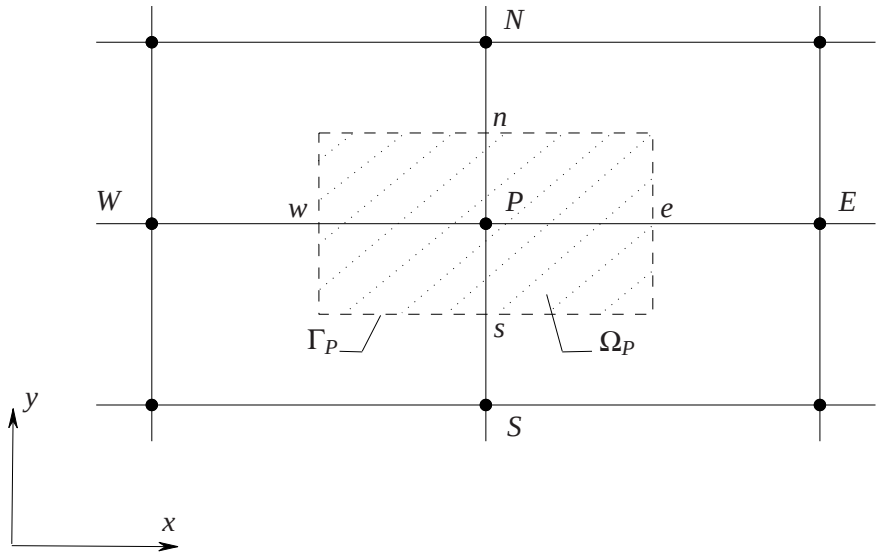

Figure 3: Schematic outline for a control-volume in 2D.

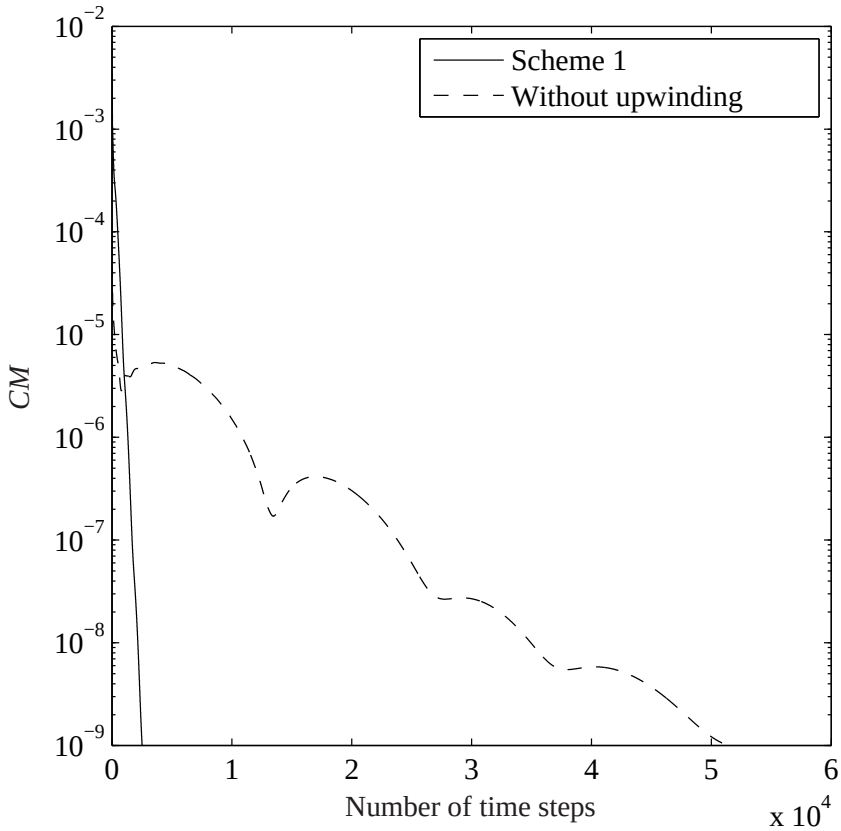

Figure 4: Lid-driven cavity flow, IRBFE-CVM, $Re = 1000$, grid $= 81 \times 81$, solution at $Re = 400$ used as initial guess: convergence behaviour. Scheme 1 using a time step of 3×10^{-4} converges remarkably faster than the no-upwind version using a time step of 7×10^{-6}. It is noted that the latter diverges for time steps greater than 7×10^{-6}. *CM* denotes the convergence measure as defined by (57).

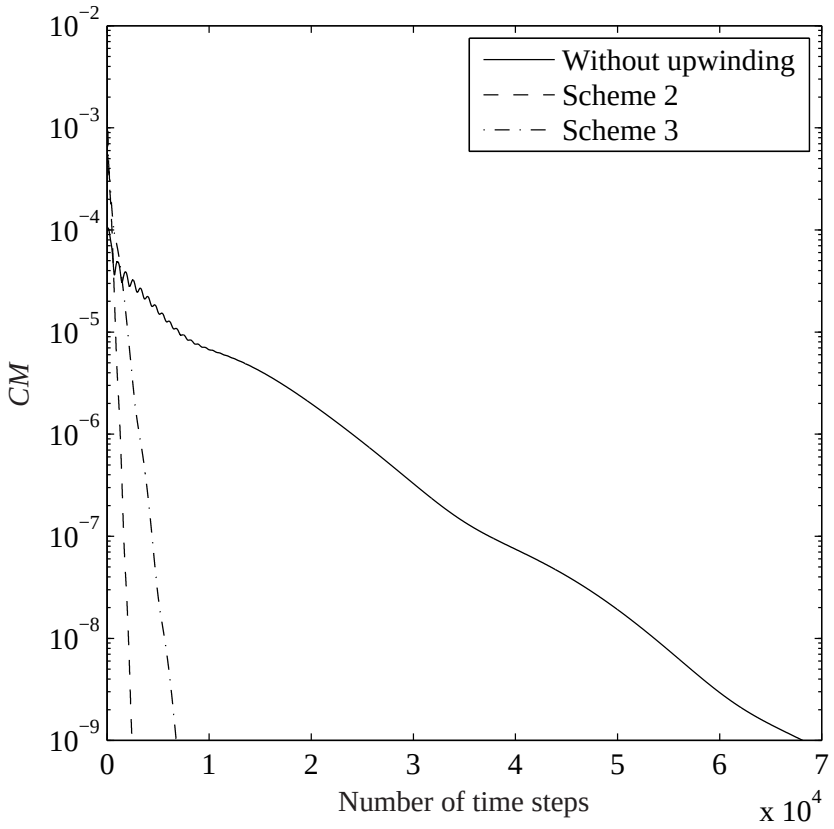

Figure 5: Lid-driven cavity flow, IRBFE-CM, $Re = 1000$, grid $= 81 \times 81$, solution at $Re = 400$ used as initial guess: convergence behaviour. Scheme 2 and Scheme 3, using a time step of 3×10^{-4} and 10^{-4}, respectively, converge remarkably faster than the no-upwind version using a time step of 8×10^{-6}. It is noted that the latter diverges for time steps greater than 8×10^{-6}. *CM* denotes the convergence measure as defined by (57).

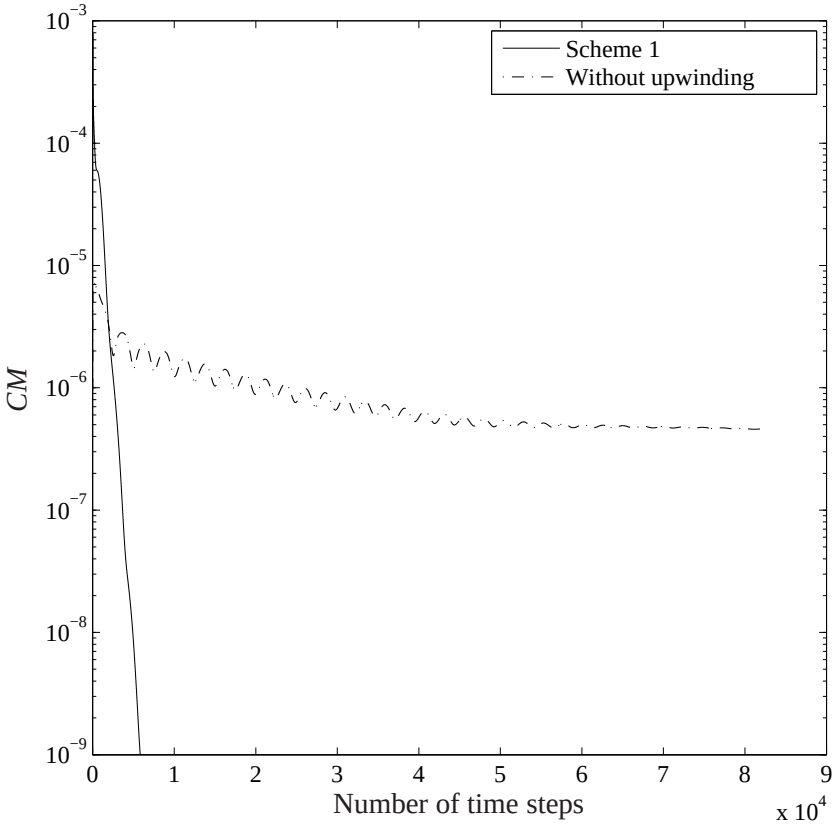

Figure 6: Lid-driven cavity flow, IRBFE-CVM, $Re = 3200$, grid $= 91 \times 91$, solution at $Re = 2000$ used as initial guess: convergence behaviour. Scheme 1 using a time step of 10^{-4} converges remarkably faster than the no-upwind version using a time step of 8×10^{-7}. It is noted that the latter diverges for time steps greater than 8×10^{-7}. *CM* denotes the convergence measure as defined by (57).

(a) $Re = 0$

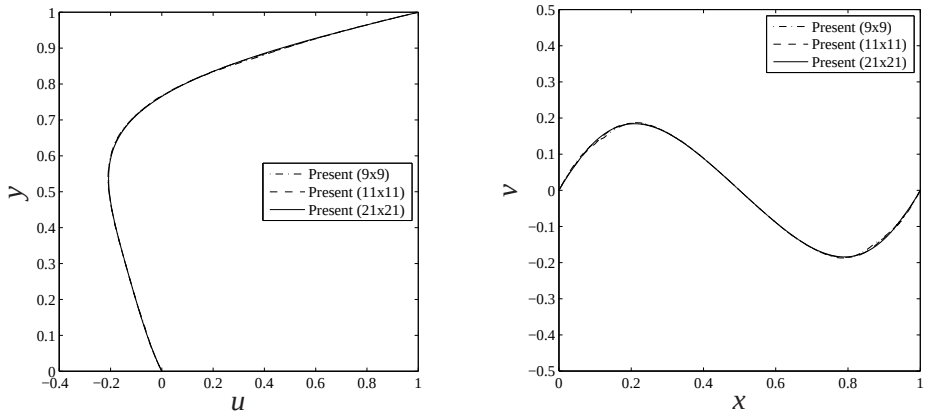

(b) $Re = 100$

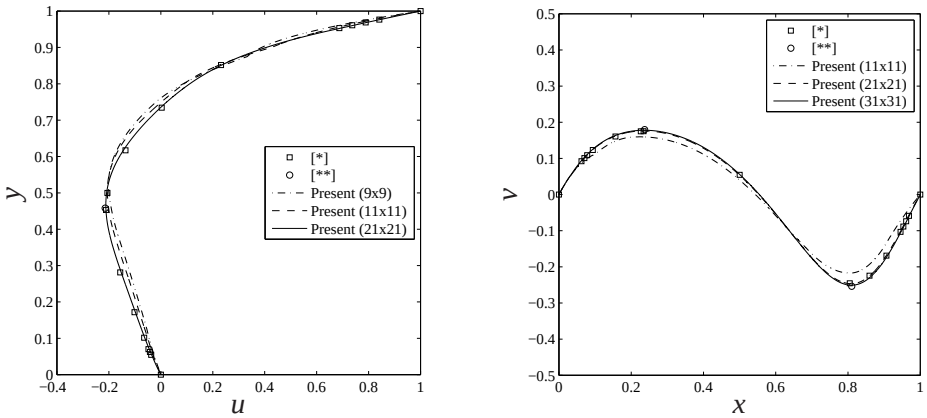

(c) $Re = 400$

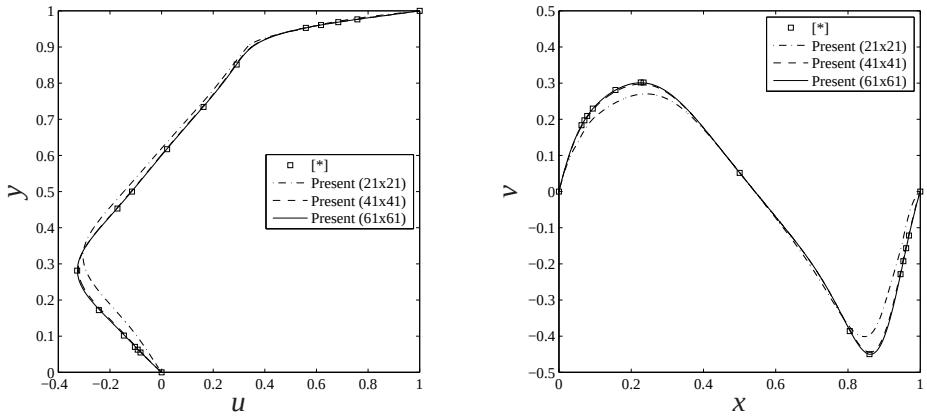

Figure 7: Lid-driven cavity flow, IRBFE-CVM: velocity profiles on the vertical (left) and horizontal (right) centrelines at different grids, results by Ghia, Ghia, and Shin (1982) were obtained at a grid of 129×129. $[*]$ is Ghia, Ghia, and Shin (1982) and $[**]$ is Botella and Peyret (1998).

(a) $Re = 1000$

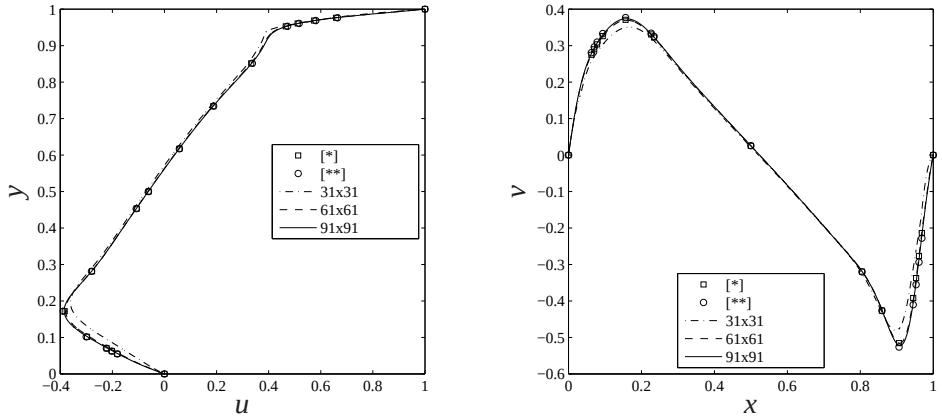

(b) $Re = 3200$

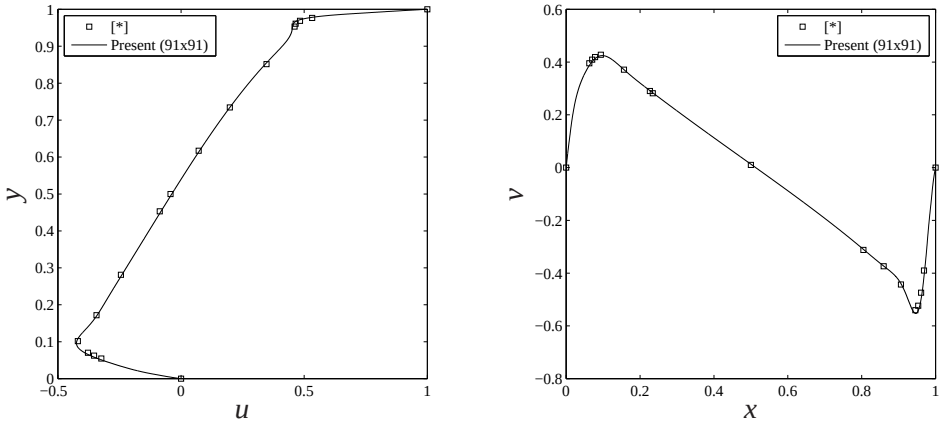

Figure 8: Lid-driven cavity flow, IRBFE-CVM: velocity profiles on the vertical (left) and horizontal (right) centrelines at different grids, results by Ghia, Ghia, and Shin (1982) were obtained at a grid of 129×129. $[*]$ is Ghia, Ghia, and Shin (1982) and $[**]$ is Botella and Peyret (1998).

(a) $Re = 0$, 61×61

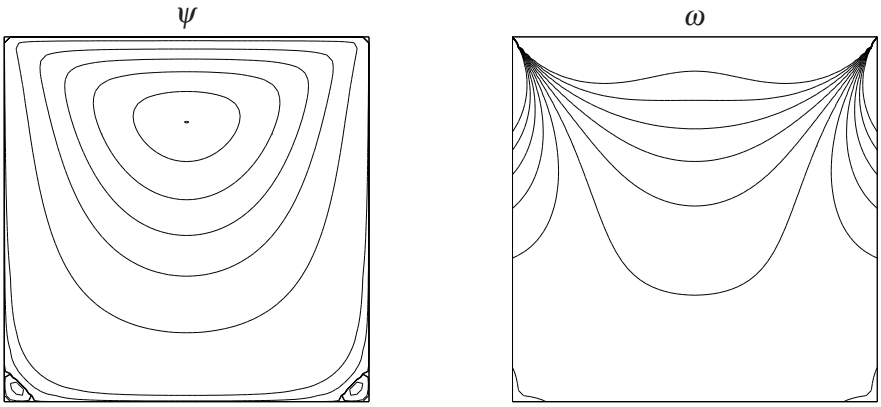

(b) $Re = 100$, 61×61

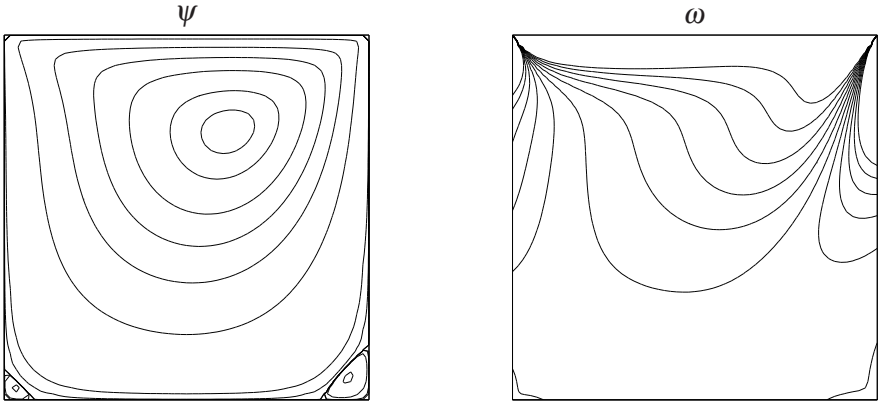

(c) $Re = 400$, 71×71

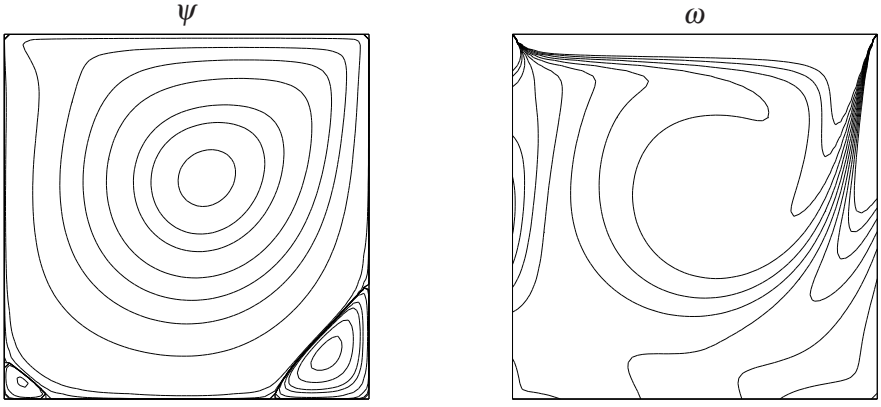

Figure 9: Lid-driven cavity flow, IRBFE-CVM: stream and iso-vorticity lines for several *Re* numbers and grid sizes. The contour values are taken to be the same as those in Ghia, Ghia, and Shin (1982) and Sahin and Owens (2003) respectively.

(a) $Re = 1000, 81 \times 81$

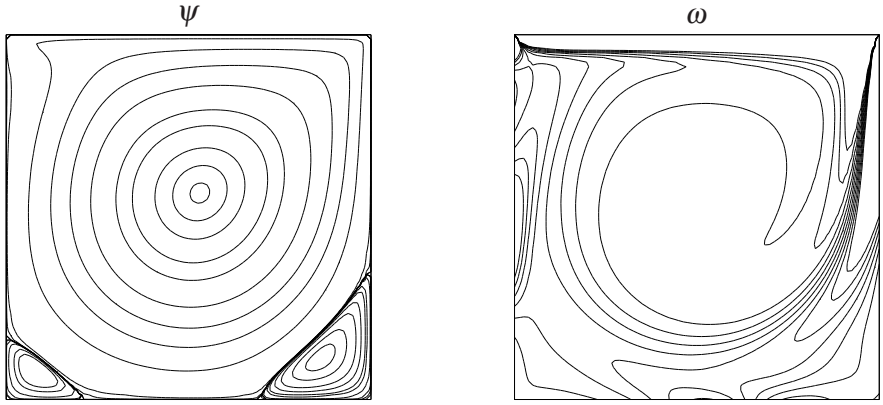

(b) $Re = 3200, 91 \times 91$

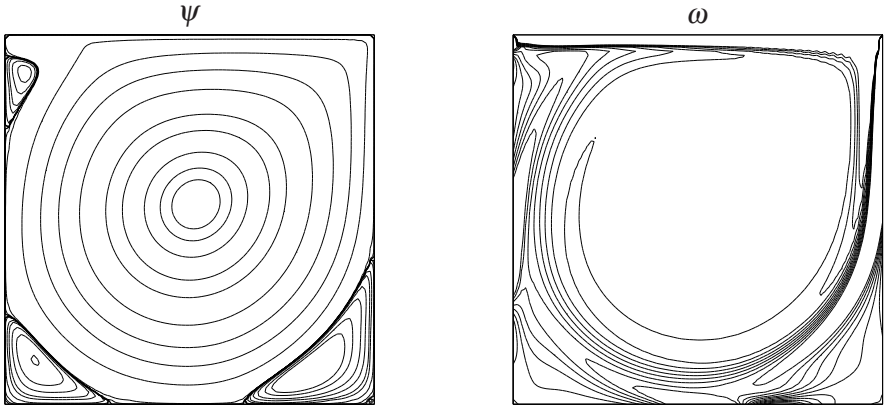

Figure 10: Lid-driven cavity flow, IRBFE-CVM: stream and iso-vorticity lines for several *Re* numbers and grid sizes. The contour values are taken to be the same as those in Ghia, Ghia, and Shin (1982) and Sahin and Owens (2003) respectively.

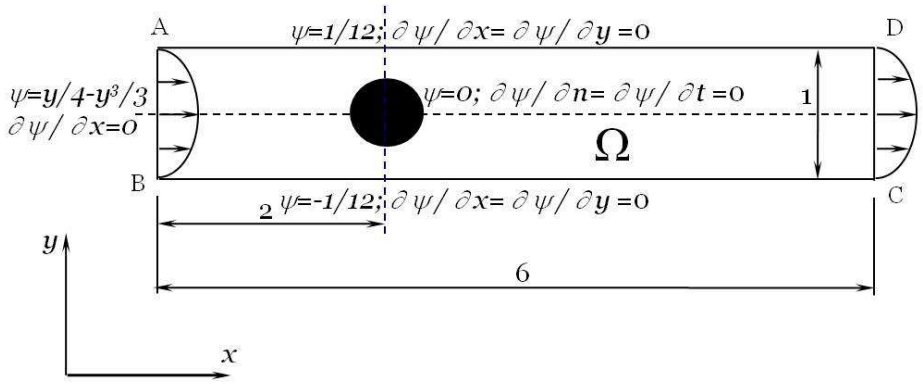

Figure 11: Flow past a circular cylinder in a channel: schematic representation of the computational domain.

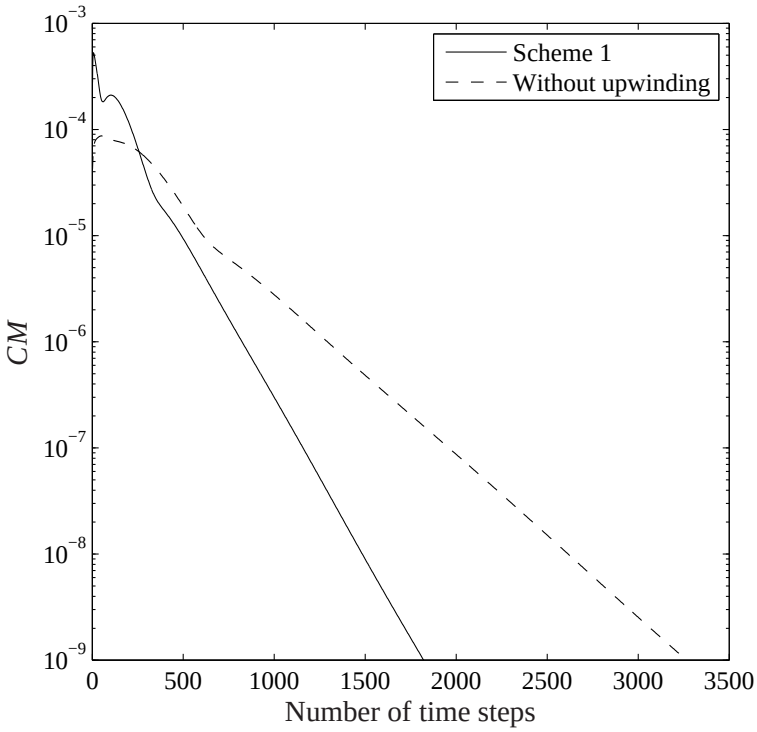

Figure 12: Flow past a circular cylinder in a channel, IRBFE-CVM, $\gamma = 0.5$, $Re = 60$, grid $= 367 \times 62$, solution at $Re = 35$ used as initial guess: convergence behaviour. Scheme 1 using a time step of 2×10^{-4} converges faster than the no-upwind version using a time step of 10^{-4}. It is noted that the latter diverges for time steps greater than 10^{-4}. *CM* denotes the convergence measure as defined by (57).

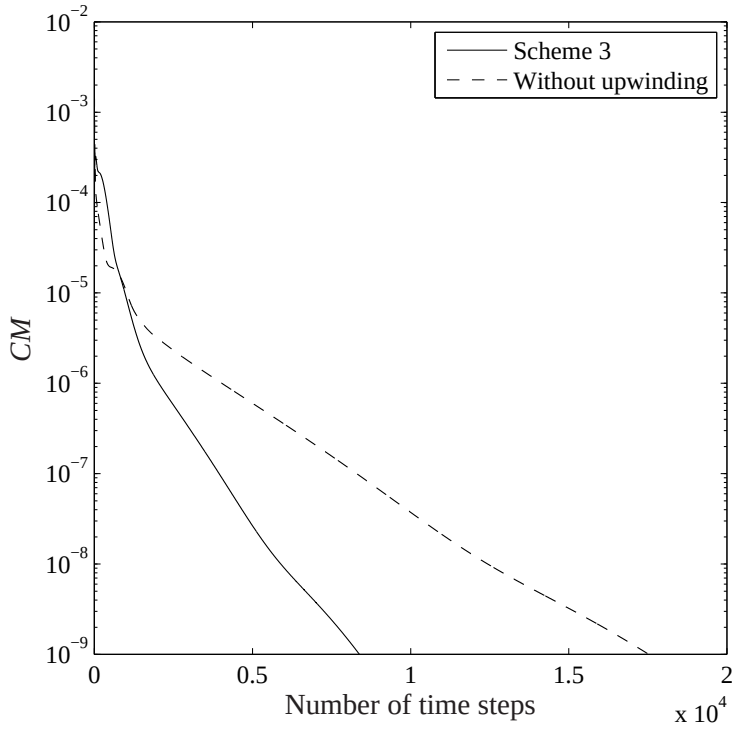

Figure 13: Flow past a circular cylinder in a channel, IRBFE-CM, $\gamma = 0.5$, $Re = 60$, grid $= 367 \times 62$, solution at $Re = 0$ used as initial guess: convergence behaviour. Scheme 3 using a time step of 10^{-4} converges faster than the no-upwind version using a time step of 5×10^{-5}. It is noted that the latter diverges for time steps greater than 5×10^{-5}. *CM* denotes the convergence measure as defined by (57).

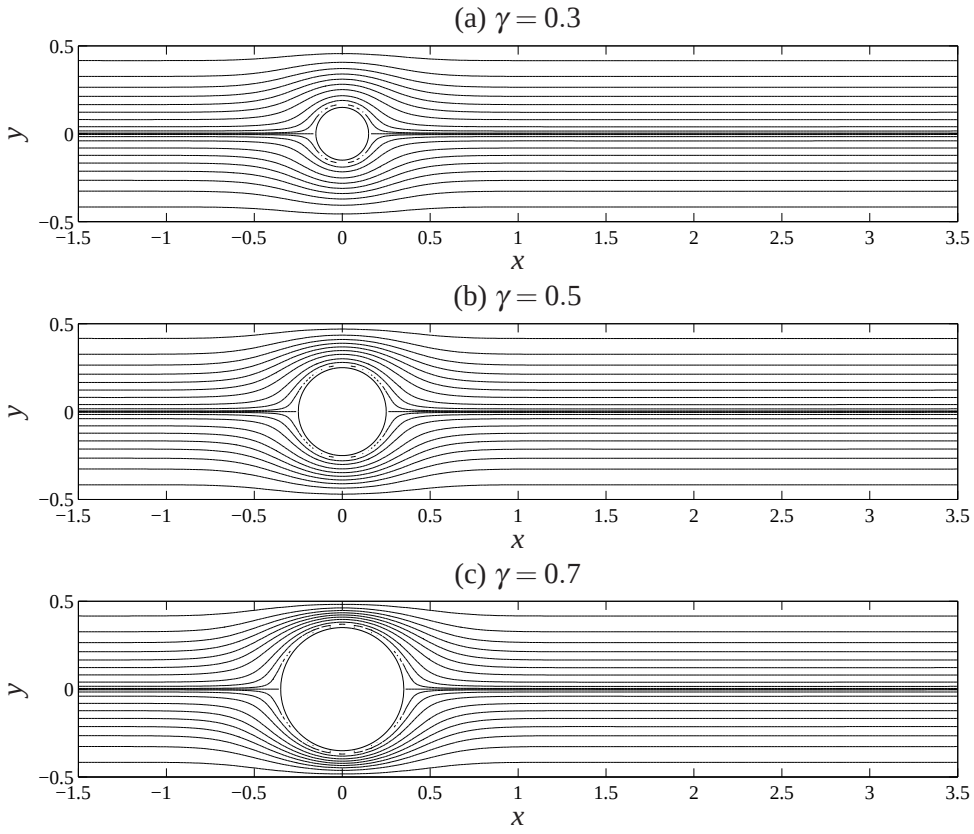

Figure 14: Flow past a circular cylinder in a channel, IRBFE-CVM, $Re = 0$, grid $= 367 \times 62$: streamlines at different values of the blockage ratio.

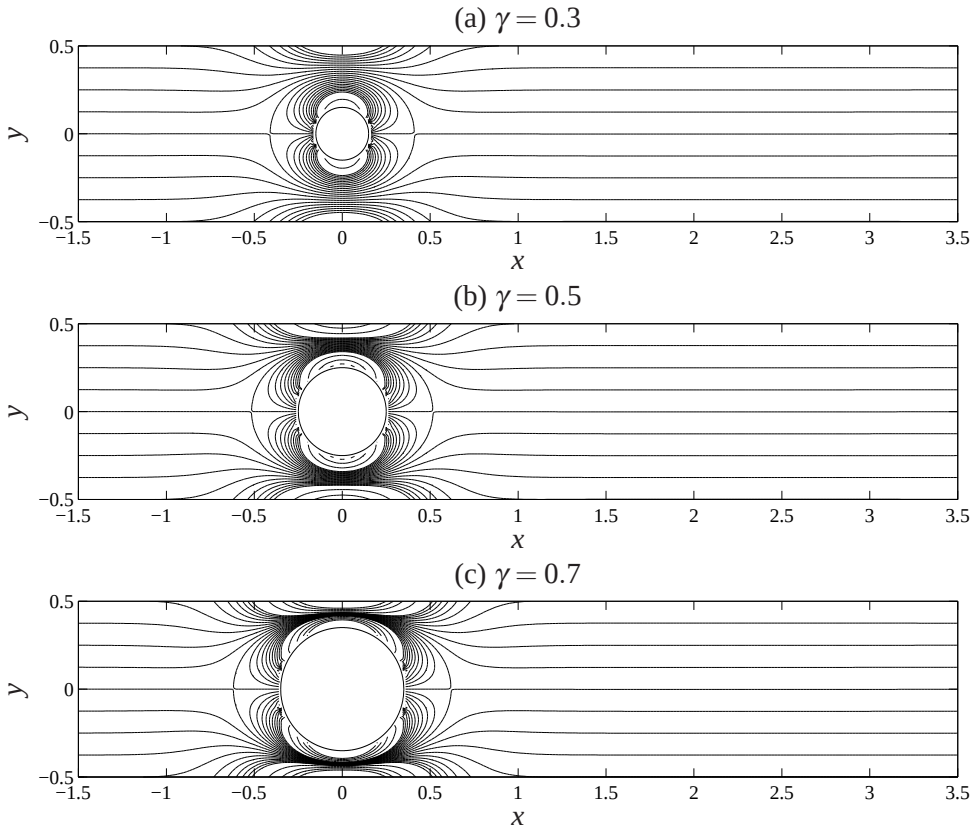

Figure 15: Flow past a circular cylinder in a channel, IRBFE-CVM, $Re = 0$, grid $= 367 \times 62$: iso-vorticity lines at different values of the blockage ratio.

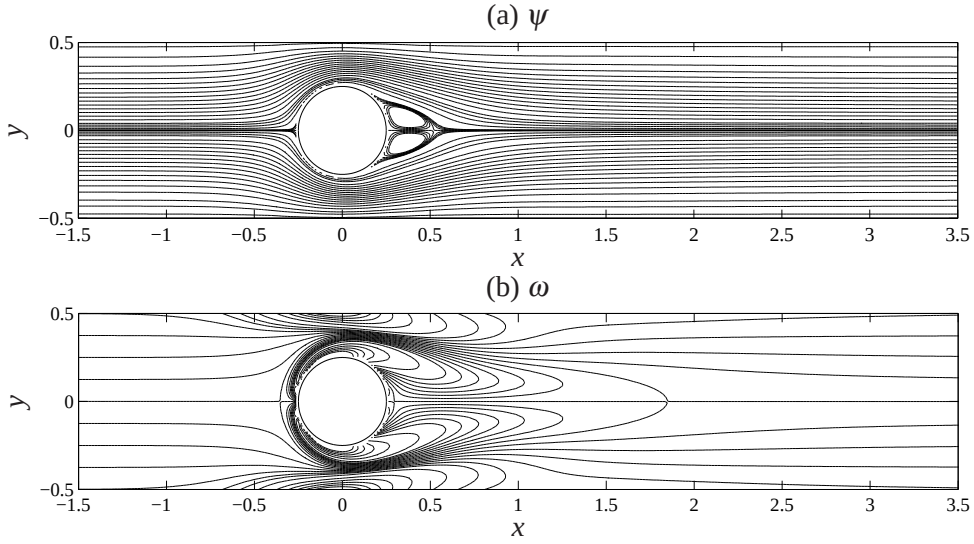

Figure 16: Flow past a circular cylinder in a channel, IRBFE-CVM, $\gamma = 0.5$, $Re = 60$, grid $= 367 \times 62$: streamlines and iso-vorticity lines.

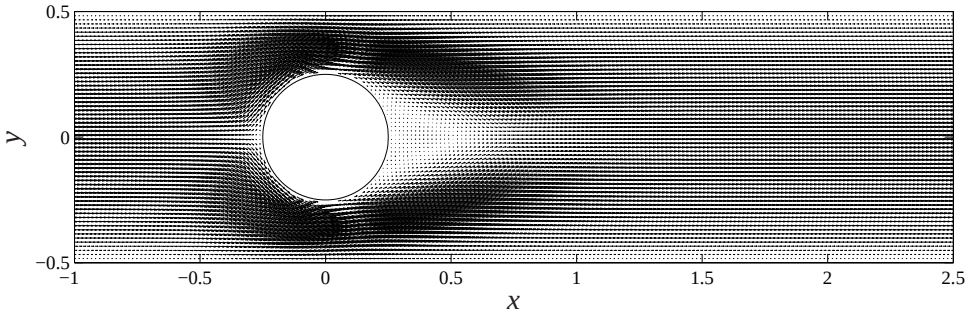

Figure 17: Flow past a circular cylinder in a channel, IRBFE-CVM, $\gamma = 0.5$, $Re = 60$, grid $= 367 \times 62$: velocity vector field.

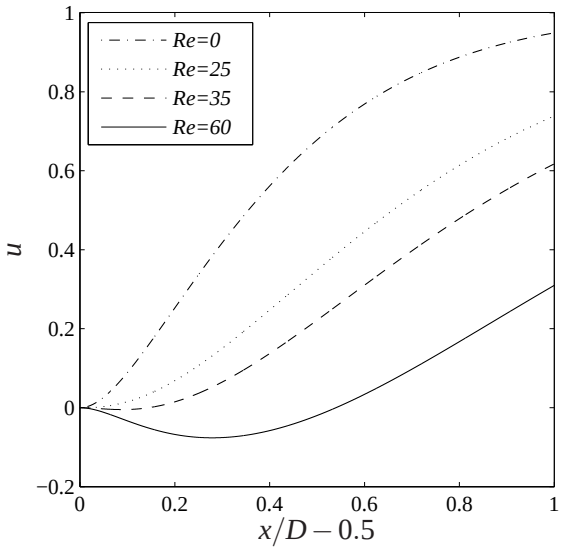

Figure 18: Flow past a circular cylinder in a channel, IRBFE-CVM, $\gamma = 0.5$: velocity profiles on the centreline behind the cylinder at different Reynold numbers.